

Impact of water saturation on seismoelectric transfer functions: a laboratory study of coseismic phenomenon

C. Bordes,¹ P. Sénéchal,¹ J. Barrière,^{1,2} D. Brito,¹ E. Normandin³ and D. Jougnot^{4,5}

¹Lab. des Fluides Complexes et leurs Réservoirs - LFC-R UMR 5150 Univ Pau & Pays Adour, CNRS, TOTAL, BP 1155 - PAU, F-64013, France.

E-mail: clarisse.bordes@univ-pau.fr

²National Museum of Natural History & European Center for Geodynamics and Seismology, Rue Josy Welter 19, L-7256 Walferdange, Luxembourg

³Univ Pau & Pays Adour, Innov Adour, PAU, F-64013, France

⁴Applied and Environmental Geophysics Group, Institute of Earth Sciences, University of Lausanne, CH-1015, Switzerland

⁵CNRS, UMR 7619, METIS, F-75005 Paris, France

Accepted 2014 December 2. Received 2014 November 28; in original form 2014 July 23

SUMMARY

Seismic waves propagating in a porous medium, under favourable conditions, generate measurable electromagnetic fields due to electrokinetic effects. It has been proposed, following experimental and numerical studies, that these so-called ‘seismoelectromagnetic’ couplings depend on pore fluid properties. The theoretical frame describing these phenomena are based on the original Biot’s theory, assuming that pores are fluid-filled. We study here the impact of a partially saturated medium on amplitudes of those seismoelectric couplings by comparing experimental data to an effective fluid model. We have built a 1-m-length-scale experiment designed for imbibition and drainage of an homogeneous silica sand; the experimental set-up includes a seismic source, accelerometers, electric dipoles and capacitance probes in order to monitor seismic and seismoelectric fields during water saturation. Apparent velocities and frequency spectra (in the kiloHertz range) are derived from seismic and electrical measurements during experiments in varying saturation conditions. Amplitudes of seismic and seismoelectric waves and their ratios (i.e. transfer functions) are discussed using a spectral analysis performed by continuous wavelet transform. The experiments reveal that amplitude ratios of seismic to coseismic electric signals remain rather constant as a function of the water saturation in the $S_w = [0.2–0.9]$ range, consistently with theoretically predicted transfer functions.

Key words: Electrical properties; Hydrogeophysics; Wave propagation.

1 INTRODUCTION

Relative fluid–solid motions induced at the microscopic scale by a seismic wave propagating in porous media generate conversions from mechanical to electromagnetic energy. This transient electrokinetic phenomenon, that can be observed at the macroscopic scale, was first theoretically described by Frenkel (1944). More recently, in a reference paper, Pride (1994) developed the all set of governing equations for the seismoelectric phenomenon in a saturated medium. These equations are based upon the Biot’s theory for seismic propagation in porous medium (Biot 1956a,b) and Maxwell’s equations for electromagnetism using a volume averaging approach. Pride’s complete seismoelectric analytical formulation has been largely used in recent years in numerical computations (Garambois & Dietrich 2002; Guan & Hu 2008; Zyserman *et al.* 2010; Santos *et al.* 2011; Zyserman *et al.* 2012; Warden *et al.* 2013) in order to discuss potential applications of seismoelectrics as a new geophysical probing method. By deriving the dispersion relations in terms of effective densities, Schakel & Smeulders (2010)

proposed an alternative approach, while confirming its consistency with the original Pride’s equations. In the last decade, seismoelectric phenomena were also discussed by considering electrokinetic couplings as a function of the charge density (e.g. Revil & Jardani 2010; Revil & Mahardika 2013; Jougnot *et al.* 2013; Revil *et al.* 2014).

Seismoelectromagnetic measurements are dominated by coseismic responses that accompanies both body and surface waves, but they also may contain signals originating from seismoelectromagnetic radiating waves generated at interfaces. It is commonly advanced that the analysis of these interfacial seismoelectromagnetic measurements may lead to informations on petrophysical properties of very thin layers (i.e. thinner than a quarter seismic wavelength). Some encouraging field measurements showed this effect to be measurable, at least for shallow interfaces (Garambois & Dietrich 2001; Dupuis *et al.* 2007; Haines *et al.* 2007a,b; Strahser *et al.* 2007) and at the ice-bed interface (Kulesa *et al.* 2006). However ‘deeper’ studies (Thompson & Gist 1993) are very rare, in particular because the interface radiation is very low in amplitude

(Dupuis & Butler 2006), despite significant improvements in signal processing (Butler & Russell 1993; Dupuis *et al.* 2009; Warden *et al.* 2012).

In the last decade, laboratory experiments performed under controlled conditions have provided several data sets on seismo-electromagnetic coseismic and interfacial signals. For example, evidences of coseismic seismomagnetic fields were shown for Stoneley (Zhu & Toksöz 2005) and body waves (Bordes *et al.* 2006, 2008). By using an apparatus designed for the characterization of fluid dispersion, Dukhin *et al.* (2010) also performed seismoelectric measurements showing that the magnitude of seismo-electromagnetic current depends on the porosity, pore sizes, zeta potential and elastic properties of the porous matrix. Other studies confirmed that the rocks petrophysical parameters (Zhu *et al.* 2000; Zhu & Toksöz 2003) and the fluid properties (Chen & Mu 2005; Block & Harris 2006) have strong effects both on the shape and on the amplitude of interfacial radiations. Schakel *et al.* (2011a,b) eventually showed that laboratory data and numerical predictions were in good agreement in terms of traveltimes, waveforms and polarity.

Although the dependence of seismo-electromagnetic signals on fluid parameters such as the pore fluid conductivity, pH or viscosity have already been numerically and/or experimentally addressed, the impact of partial saturation has been rarely studied. However, saturation is often not achieved in reservoirs, since those generally contain at least a few percents of gas or oil, strongly influencing mechanical (Bachrach & Nur 1998; Bachrach *et al.* 1998; Rubino & Holliger 2012) and electric properties of the rock (Archie 1942). Strahser *et al.* (2011) measured both seismo-electric coupling and electric impedance between electrodes and suggested that the water content should modify seismo-electromagnetic couplings. To our knowledge, the only laboratory experiment was performed by Parkhomenko & Tsze-San (1964) who measured the seismo-electric potential during water imbibition of dried rocks. Their results showed a dependence of the seismo-electric effect on water content, but they did not measure seismic displacements nor acceleration, assuming that it should not vary with a reproducible seismic source. Nevertheless, numerous later experimental and theoretical studies showed that attenuation of seismic waves depends on the water saturation (Santos *et al.* 1990; Mavko & Nolen-Hoeksema 1994; Tuncay & Corapcioglu 1996; Carcione 2001; Lo *et al.* 2005; Masson & Pride 2007; Lebedev *et al.* 2009; Rubino & Holliger 2012). As a consequence, the dependence of seismo-electric coupling must be addressed in term of transfer function to account for seismic amplitudes variations due to changes in water saturation.

The goal of this paper is to compare laboratory data with the theoretical predictions from the Pride's theory (1994), extended to partial saturation by an effective fluid model as proposed in Warden *et al.* (2013). In Section 2, we derive the low frequency and dynamic analytical transfer functions giving the ratio of the local coseismic seismo-electric field to the local acceleration using the Pride & Haartsen (1996) approach. We present in Section 3 the experimental set-up which consists of a 1-m-typical-length-scale container filled with an homogeneous silica sand. Imbibition and drainage were performed in this container while seismic and seismo-electric signals were recorded. A spectral analysis based on a continuous wavelet transform (CWT) presented in Section 4 is then applied to the experimental signals and the results are compared to theoretical predictions. Our conclusion on the impact of saturation on seismo-electric coupling is given in Section 5.

2 THEORETICAL BACKGROUND

2.1 Seismo-electric transfer functions in fluid-filled media

Following Pride's original study (1994), Pride & Haartsen (1996) developed the analytical formulation of the coseismic transfer functions giving the seismo-electric field vector \mathbf{E} as a function of the grain acceleration associated to compressional P waves and shear S waves. By assuming plane waves with an $e^{-i\omega t}$ dependence in time (t is time and ω is the wave pulsation), the grain acceleration of P and S waves $\ddot{\mathbf{U}}_i(\omega)$ can be linked to the displacement $\mathbf{U}_i(\omega)$ following:

$$\mathbf{U}_i(\omega) = -\frac{\ddot{\mathbf{U}}_i(\omega)}{\omega^2} \quad \text{with} \quad i = P, S. \quad (1)$$

By neglecting the presence of Biot's slow waves, the dynamic coseismic seismo-electric field can be written as a function of P and S accelerations following:

$$\mathbf{E}(\omega) = \psi_{P\text{-dyn}}(\omega)\ddot{\mathbf{U}}_P(\omega) + \psi_{S\text{-dyn}}(\omega)\ddot{\mathbf{U}}_S(\omega), \quad (2)$$

where $\psi_{P\text{-dyn}}$ and $\psi_{S\text{-dyn}}$ are, respectively, defined as the complex dynamic transfer functions for (fast) P and S waves defined by:

$$\psi_{P\text{-dyn}}(\omega) = \frac{i}{\omega} \frac{\tilde{\rho}(\omega)L(\omega)}{\tilde{\varepsilon}(\omega)} \frac{Hs_P^2(\omega) - \rho}{Cs_P^2(\omega) - \rho_f} \quad (3)$$

and

$$\psi_{S\text{-dyn}}(\omega) = \frac{i}{\omega} \mu \tilde{\rho}(\omega)L(\omega) \frac{G}{\rho_f s_S^2(\omega) - \mu \tilde{\varepsilon}(\omega)}. \quad (4)$$

In eqs (3) and (4), μ is the magnetic permeability ($\mu = \mu_0 = 4\pi 10^{-7} \text{ V s A}^{-1} \text{ m}^{-1}$ in non-metallic rocks), $\tilde{\rho}$ is the effective density of the fluid in relative motion, L is the coupling coefficient, $\tilde{\varepsilon}$ is the effective electrical permittivity of the porous medium, ρ is the bulk density of the porous medium depending, respectively, on grain density ρ_s , fluid density ρ_f and on porosity ϕ . s_P and s_S are, respectively, the complex slowness of (fast) P and S waves, and H , C and G are poroelastic moduli of the medium. The complete set of equations used in this paper are shown in Appendix A.

By comparing seismic and seismo-electric signals from a field study, Garambois & Dietrich (2001) showed that $\mathbf{E}(\omega)$ and $\ddot{\mathbf{U}}(\omega)$ should be proportional at 'low' frequencies and for fast P waves. This approximation assumes that electromagnetic fields are in the diffusive regime and that seismic frequencies are much lower than the Biot's frequency f_c (Biot 1962) defined by

$$f_c = \frac{\phi \eta_f}{2\pi \gamma_0 \rho_f k_0} = \frac{\omega_c}{2\pi}, \quad (5)$$

where η_f is the dynamic viscosity of the fluid, k_0 is the intrinsic permeability of the medium and ω_c is the wave pulsation at the Biot's frequency. The tortuosity γ_0 in eq. (5) is estimated here by the relation proposed by Berryman (1981) $\gamma_0 = (1-r)(1+\frac{1}{\phi})$ where r depends on the grain shape ($0 < r < 1$ for ellipsoidal grains and $r = 0.5$ for spherical grains).

For frequencies lower than f_c , Garambois & Dietrich (2001) neglected the dynamic behaviour of electrical properties, permeability and electrokinetic coupling. They deduced that the low frequency seismo-electric field \mathbf{E}_P associated to P waves is linearly dependent on seismic grain acceleration and that the low-frequency static transfer function $\psi_{P\text{-lf}}$ does not depend on the frequency:

$$\mathbf{E}_P(\omega) = \psi_{P\text{-lf}}\ddot{\mathbf{U}}_P(\omega) \quad \text{for } \omega \ll \omega_c \quad (6)$$

Table 1. Definition and values of the physical parameters involved in the computations of the transfer functions in a water saturated silica sand.

Physical parameter	Notation	Value	Units	
Fluid				
Density	ρ_f	10^3	kg m^{-3}	
Dynamic viscosity	η_f	10^{-3}	Pa s	
Elastic modulus	K_f	2.5×10^9	Pa	
Electrical conductivity	σ_f	1.17×10^{-2}	S m^{-1}	Measured
Solid (silica sand grains)				
Grain density	ρ_s	2.65×10^3	kg m^{-3}	
Elastic modulus	K_s	3.6×10^{10}	Pa	
Porous medium				
Porosity	ϕ	0.4		Measured
Intrinsic permeability	k_0	1.02×10^{-11}	m^2	Measured
Tortuosity	γ_0	1.75		From Berryman (1981)
Drained or frame modulus	K_D	2.5×10^7	Pa	From seismic velocities
Shear frame modulus	G	1.54×10^7	Pa	
Pore space term	m	6		From Pride (1994)
Electrokinetic coefficient	C_{ek}	-1.73×10^{-6}	V Pa^{-1}	From Guichet <i>et al.</i> (2003), see Appendix B

with

$$\psi_{P\text{-lf}} = -\frac{\varepsilon_0 \varepsilon_f \zeta}{\eta_f \sigma_f} \rho_f \left(1 - \frac{\rho}{\rho_f} \frac{C}{H}\right) = \psi_0 \left(1 - \frac{\rho}{\rho_f} \frac{C}{H}\right), \quad (7)$$

where ζ is the zeta-potential (defined as the static electrical potential at the shear plane when a part of the diffuse layer is transported by fluid flow), ε_0 and ε_f are, respectively, the vacuum permittivity and fluid's dielectric permittivities ($\varepsilon_0 = 8.854 \times 10^{-12} \text{ F m}^{-1}$), and σ_f is the electrical fluid conductivity. Garambois & Dietrich (2001) and Strahser *et al.* (2011) suggested that the terms in parenthesis in eq. (7) could be neglected leading to $\psi_{P\text{-lf}} \simeq \psi_0$. We will discuss in the following the degree of validity of the transfer function $\psi_{P\text{-lf}} = \psi_0$ obtained thanks to this simplification.

Using the same hypotheses as Garambois & Dietrich (2001), we obtain similarly from eq. (4) a low frequency transfer function for shear S waves

$$\mathbf{E}_S(\omega) = \psi_{S\text{-lf}}(\omega) \ddot{\mathbf{U}}_S(\omega) \quad \text{for } \omega \ll \omega_c \quad (8)$$

with

$$\psi_{S\text{-lf}}(\omega) = i \frac{\varepsilon_0 \varepsilon_f \zeta}{\eta_f} \frac{\mu}{\omega} \frac{G}{\rho} \frac{\phi}{\gamma_0}. \quad (9)$$

We notice in eq. (9) that $\psi_{S\text{-lf}}$ inversely depends on ω whereas $\psi_{P\text{-lf}}$ is independent of the wave pulsation. Garambois & Dietrich (2001) get a similar result for the formulation of the seismomagnetic transfer function and chose to express the magnetic field versus the grain velocity in order to avoid this frequency dependence.

At this point, it is more convenient to introduce the electrokinetic coupling coefficient

$$C_{ek} = \frac{\varepsilon_0 \varepsilon_f \zeta}{\eta_f \sigma_f} \quad (10)$$

(see Appendix B for a more complete discussion on C_{ek}) defined by electrofiltration measurements (Jouniaux & Pozzi 1995; Guichet *et al.* 2003, 2006). Using C_{ek} in eqs (2), (7) and (9) eventually leads to the low frequency expression of the coseismic seismoelectric

field:

$$\begin{aligned} \mathbf{E}(\omega) &= \psi_{P\text{-lf}} \ddot{\mathbf{U}}_P(\omega) + \psi_{S\text{-lf}}(\omega) \ddot{\mathbf{U}}_S(\omega) \\ &= -C_{ek} \rho_f \left[\left(1 - \frac{\rho}{\rho_f} \frac{C}{H}\right) \ddot{\mathbf{U}}_P(\omega) - i \frac{\mu}{\omega} \frac{G}{\rho} \frac{\phi}{\gamma_0} \sigma_f \ddot{\mathbf{U}}_S(\omega) \right] \\ &\quad \text{for } \omega \ll \omega_c. \end{aligned} \quad (11)$$

Using the hypotheses and equations developed in Appendix A as well as the physical values given in Table 1, we have computed the low frequency and dynamic transfer functions in a fluid-filled (saturated) silica sand from eqs (2)–(4), (7) and (9). Fig. 1 shows magnitudes and phase angles of the P - and S -waves transfer functions. In these fluid-filled sand simulations, which properties were chosen consistently with the experiment presented below, the Biot's frequency is $f_c = 3570 \text{ Hz}$.

The main information in Fig. 1 is that the predicted $|\mathbf{E}_S/\ddot{\mathbf{U}}_S|$ ratios are tiny compared to the $|\mathbf{E}_P/\ddot{\mathbf{U}}_P|$ (factor at most 10^{-6} between those two ratios). Even if the measurements of a seismoelectric field in a transverse direction compared to the main longitudinal P -wave direction may be of interest, the analysis of such small transfer functions in S waves seems out of reach both numerically and experimentally as already foreseen by Garambois & Dietrich (2001). Note also that as indicated by eq. (11), the coseismic seismoelectric fields associated to P and S waves are phase shifted by an angle $\pi/2$ as seen in Figs 1(b) and (d). We conclude that the global ratio $|\mathbf{E}/\ddot{\mathbf{U}}|$ is useless as soon as P and S waves coexist in the seismic signal, since only the P waves are efficiently converted into electric field: the magnitude of the ratio $|\mathbf{E}/\ddot{\mathbf{U}}|$ is shifted towards smaller values compared to the analytical P transfer function $\psi_{P\text{-dyn}}$ when S waves are present.

Computations in Fig. 1 confirm that the low frequency approximations $\psi_{P\text{-lf}}$ and $\psi_{S\text{-lf}}$ are consistent with the dynamic transfer functions $\psi_{P\text{-dyn}}$ and $\psi_{S\text{-dyn}}$ as long as the current frequency is below the Biot's frequency (Garambois & Dietrich 2001). This behaviour is in good agreement with experimental measurements of frequency dependent coupling coefficients (Reppert *et al.* 2001; Tardif *et al.* 2011). For $f \gg f_c$, the magnitude of the dynamic transfer function for P waves strongly decreases as the frequency increases. It is also worth to notice in Figs 1(a) and (b) that although the computation for $f \ll f_c$ of the simplified low frequency transfer function ψ_0 gives a correct magnitude (within 3 percents) compared to $\psi_{P\text{-dyn}}$

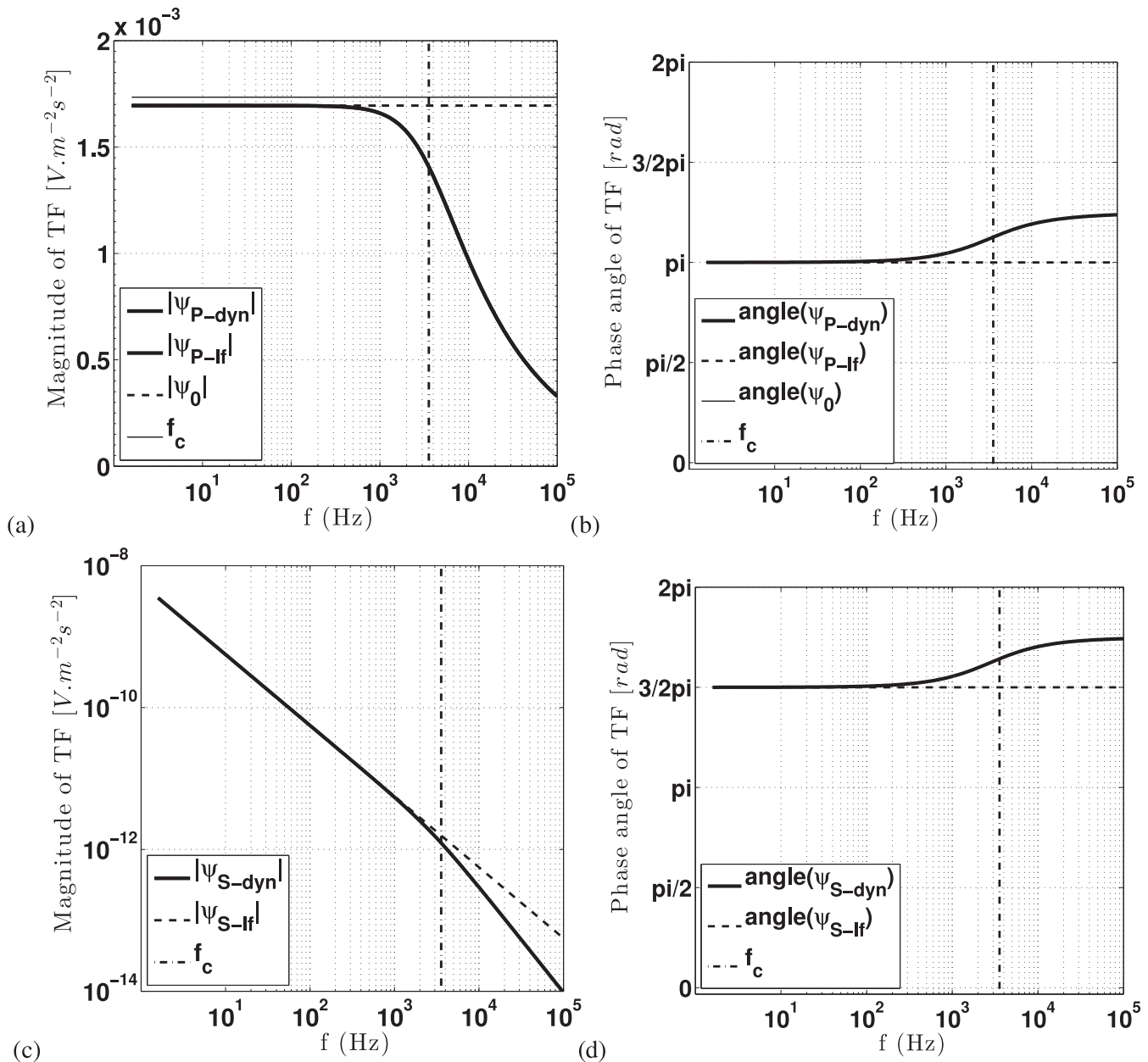


Figure 1. Magnitude (a) and phase angles (b) as a function of the frequency f , respectively for the P -waves dynamic transfer function $\psi_{P\text{-dyn}}$, for the P -waves low frequency transfer function $\psi_{P\text{-lf}}$ and for the P -waves simplified low frequency transfer function ψ_0 in a saturated sand (formulation in Appendix A and physical parameters in Table 1). Panels (c) and (d) are the magnitudes and phase angles of the S -waves transfer functions ($\psi_{S\text{-dyn}}$ and $\psi_{S\text{-lf}}$) for the same parameters of the computations shown in (a) and (b). The Biot's frequency f_c is shown with a vertical dashed line on all graphs.

or $\psi_{P\text{-lf}}$ formulations, ψ_0 is phase shifted by π compared to $\psi_{P\text{-dyn}}$ or $\psi_{P\text{-lf}}$. As a consequence, the seismoelectric signals predicted by the simplified low frequency transfer function ψ_0 have to be used cautiously since it may lead to some misinterpretations regarding the polarity of the seismic signal compared to electrical signal.

2.2 The effective fluid model

The theoretical transfer functions shown in Section 2.1 were developed for fluid-filled porous media since they were based on the original Biot's formulation. However, partial saturation has a strong impact on both seismic propagation and electrokinetic coupling. As

long as the seismic wavelengths are much larger than the fluid heterogeneities, the simplest way to account for this partial saturation is to use effective fluid models as basically performed in seismic surveys (Bachrach & Nur 1998) or laboratory measurements (Barrière *et al.* 2012).

For this purpose, the terms ρ_f , ρ , C , H , σ_f and C_{ek} in eqs (3), (4) (dynamic formulation) and (11) (low frequency formulation) are replaced by their effective values depending on the water saturation S_w (defined as the pore volume ratio filled with water). The details of this classic effective model are given in Appendix A. Several models of electrokinetic coefficient $C_{ek}(S_w)$ accounting for partial saturation were constructed from theoretical studies and/or laboratory measurements (Guichet *et al.* 2003; Darnet & Marquis

Table 2. List of the various functions $f(S_w)$ used in the electrokinetic coefficient depending on saturation $C_{ek}(S_w) = C_{ek}(S_w = 1)f(S_w)$. The various used notations are detailed in Appendix B.

Model	$f(S_w)$	Reference
Linear model	S_e	Guichet <i>et al.</i> (2003)
Volume averaging	$S_e^{\frac{2+3\lambda}{\lambda}} / S_w^{n+1}$	Revil <i>et al.</i> (2007)
Capillary tubes	S_e / S_w^n	Jackson (2010)

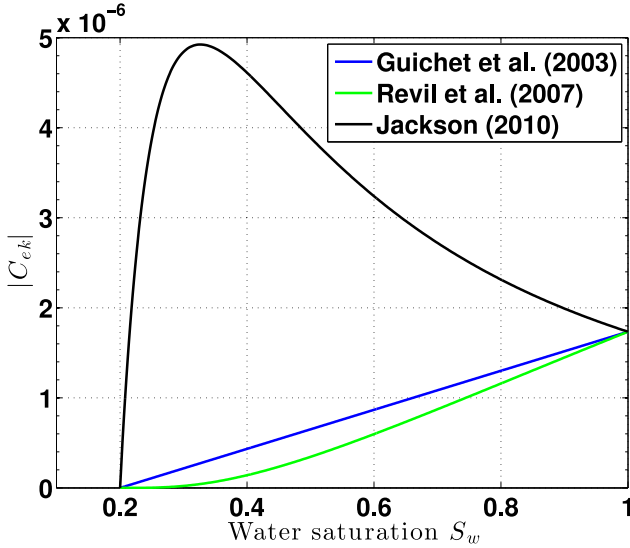


Figure 2. Absolute values of the coupling electrokinetic coefficients $|C_{ek}(S_w)|$ as a function of the water saturation S_w , for different electrokinetic models. The analytical formulations of the models are shown explicitly in Appendix B.

2004; Revil & Cerepi 2004; Revil *et al.* 2007; Allègre *et al.* 2010, 2012; Jackson 2010). The Biot frequency ω_c is therefore strongly affected via its dependence on $\rho_f(S_w)$ and $\eta_f(S_w)$. The various $C_{ek}(S_w)$ models used in this study are described in Appendix B; all the electrokinetic models can be written under the following expression $C_{ek}(S_w) = C_{ek}(S_w = 1)f(S_w)$ where $f(S_w)$ are listed in Table 2 for the different models. The way we have derived the saturated value of $C_{ek}(S_w = 1)$ is also detailed in Appendix B.

Computations of the $C_{ek}(S_w)$ models presented in Fig. 2 in the $S_w = [0.2 - 1]$ range show that, using the parameters of our experiment, two main trends are expected: Guichet *et al.* (2003) and Revil *et al.* (2007) models predict an increase of $C_{ek}(S_w)$ when S_w increases, whereas Jackson (2010) model predicts the opposite behaviour. Indeed, the choice of the electrokinetic model $C_{ek}(S_w)$ is rather important since C_{ek} amplitudes can vary by a factor of ten between various models in the considered saturation range.

We will discuss in the following the effect of water saturation on seismoelectric transfer functions amplitudes. Since the use of all these models at once would make our discussion more complex, we propose to use the model of Jackson (2010), $C_{ek}(S_w) = C_{ek}(S_w = 1)S_e S_w^{-n}$, as a reference, since it predicts values close to the experimental measurements presented in Section 4.

2.3 Seismoelectric transfer functions in partially saturated sands

We have presented in Section 2.1 both the dynamic and low frequency transfer functions in a fluid-filled silica sand. We have used

the effective properties of the fluid and electrokinetic models to rewrite key terms depending on the water saturation in Section 2.2. The physical parameters needed to express the transfer functions as a function of partial saturation are listed in Table 3.

Using the hypotheses of the calculation detailed in Appendix A, Fig. 3 presents magnitudes and phase angles of the partial saturation transfer function $\psi_{P-dyn}(S_w, \omega)$, $\psi_{P-If}(S_w)$, $\psi_0(S_w)$ as a function of the water saturation. We clearly see that the Biot's frequency (white line in Fig. 3a), varies significantly in the $S_w = [0-1]$ range. Fig. 3(a) displays the evolution of the magnitude $|\psi_{P-dyn}(S_w, \omega)|$ in a colourmap representation as a function of the saturation and the frequency: it shows that, using the Pride's theory (1994) extended to effective fluid models with Jackson (2010) model, the magnitude of the dynamic transfer function is expected to remain rather constant in the $S_w = [0.2-0.9]$ saturation range. Note that the choice of the $C_{ek}(S_w)$ model (among the ones seen in Appendix B and in Table 2) can affect the shape of the magnitude of $\psi_{P-dyn}(S_w)$ from a clear increase to a rather constant behaviour (see the solid black, blue and green curves of Fig. 3b, respectively obtained by using Jackson 2010; Guichet *et al.* 2003; Revil *et al.* 2007).

For very high saturations (close to $S_w = 1$), $|\psi_{P-dyn}(S_w, \omega)|$ strongly decreases towards 0 before a final increase to the value of the saturated transfer function described in Section 2.1. This effect is even better seen in Figs 3(b) and (c) which shows the magnitudes and phase angles of the transfer functions ψ_{P-dyn} , ψ_{P-If} , ψ_0 at a particular frequency $f = 1.5$ kHz (close to the experimental measurements presented in Section 3). Minimum values of $|\psi_{P-dyn}|$ and $|\psi_{P-If}|$ in Fig. 3(b) corresponds to the specific saturation ($S_w \simeq 0.99$) where important changes occur in the transfer function close to $S_w = 1$, originating from strong changes in the poroelastic moduli K_U , H and C (Bachrach & Nur 1998). Since the term involving the poroelastic moduli contribution was neglected in the expression of the simplified low frequency transfer function ψ_0 (see eq. 7), $\psi_0(S_w)$ does not quite follow the amplitudes of the complete expression $\psi_{dyn}(S_w)$, leading to the conclusion that ψ_0 should not be used in partially saturated media.

The low frequency transfer function $\psi_0(S_w)$ is expected to increase rapidly in the $S_w = [0.2-0.3]$ range whereas $\psi_{dyn}(S_w)$ increases more gradually. Eventually, dynamical effect at 1.5 kHz are expected to be very strong [i.e. $\psi_{P-dyn} \gg \psi_0(S_w)$] in the $S_w = [0.3-0.8]$ since the considered frequency is higher than the Biot frequency (Fig. 3a).

In order to summarize Section 2, the computations performed for a silica sand indicate that:

(i) The predicted $|\mathbf{E}_i/\ddot{\mathbf{U}}_i|$ ratios are at least 10^6 times higher for P waves than for S waves. We then conclude with two points: (1) the S waves being converted very poorly into electric field, it is hopeless both numerically and experimentally to work with an S -wave seismoelectric field; (2) if one wants to use quantitatively the amplitude of transfer P -waves functions ψ_{P-dyn} , the seismic signal should be purely composed of P waves otherwise the measured magnitude $|\mathbf{E}_P/\ddot{\mathbf{U}}_P|$ would be underestimated.

(ii) Using the Jackson (2010) model for electrokinetic coupling, the theoretically predicted $|\mathbf{E}_P(S_w, \omega)/\ddot{\mathbf{U}}_P(S_w, \omega)|$ does not vary significantly in the saturation range $S_w = [0.2-0.9]$.

(iii) Working in the kiloHertz range, low frequency approximation may overestimate $|\mathbf{E}_P/\ddot{\mathbf{U}}_P|$ ratios especially for saturations close to $S_w = 0.4$.

In the next section of the paper, we present a laboratory experiment designed to record seismoelectric data during variations of water saturation. The goal of this experiment is to address the question

Table 3. Definition and values of the physical parameters involved in the computations of the transfer functions in a partially saturated silica sand. $f(S_w)$, entering in the definition of $C_{ek}(S_w)$, are given in Table 2.

Physical parameter	Notation	Value	Units	
Fluid (water and gas)				
Density	ρ_w	10^3	kg m^{-3}	
Dynamic viscosity	η_w	10^{-3}	Pa s	
Elastic modulus	K_w	2.5×10^9	Pa	
Electrical conductivity	σ_w	1.17×10^{-2}	S m^{-1}	Measured
Gas density	ρ_g	1.2	kg m^{-3}	
Dynamic viscosity	η_g	10^{-5}	Pa s	
Elastic modulus of air	K_g	1.5×10^5	Pa	
Solid (silica sand grains)				
Grain density	ρ_s	2.65×10^3	kg m^{-3}	
Elastic modulus	K_s	3.6×10^{10}	Pa	
Porous medium				
Porosity	ϕ	0.4		Measured
Intrinsic permeability	k_0	1.02×10^{-11}	m^2	Measured
Tortuosity	γ_0	1.75		From Berryman (1981)
Drained or frame modulus	K_D	2.5×10^7	Pa	From Walton (1987), checked on seismic velocities
Shear frame modulus	G	1.54×10^7	Pa	
Electrokinetic coefficient	$C_{ek}(S_w)$	$-1.73 \times 10^{-6} \times f(S_w)$	V Pa^{-1}	From Guichet <i>et al.</i> (2003), see Appendix B
Residual water saturation	S_{w0}	0.2		
Pore space term	m	6		From Pride (1994)
Second exponent of Archie's law	n	2.58		From Doussan & Ruy (2009)
Curve shape parameter	λ	1.7		From Revil <i>et al.</i> (2007)

of the validity of the transfer functions by comparing measured $|\mathbf{E}_p/\dot{\mathbf{U}}_p|$ ratio to theoretical predictions.

3 EXPERIMENTAL SET-UP

3.1 Description of the experimental set-up

Our experimental apparatus (Barrière *et al.* 2012) described below was built to measure seismic and coseismic fields for various water content in a very permeable and homogeneous medium. A necessary condition to observe properly the propagation of direct P waves is to get at least several wavelengths along the sample length. The porous medium is a sand extracted from a sandpit located in the Landes forest (South West of France), composed of 99 per cent of quartz, which main grain size is around 250 μm). The very low seismic velocities in uncompacted sand involve short wavelengths that enable to built reasonably sized experiments (1-m length-scale container).

The final device shown in Fig. 4 was composed of:

(i) A wood container filled with uncompacted sand (34 cm \times 35 cm \times 107 cm) which bottom and lateral edges were covered by acoustic foam (Strasonic foam, Paulstra) to attenuate refracted and reflected seismic waves.

(ii) Five wells consisting of unperforated PVC pipes: imbibition was performed by injecting water under the effect of gravity through the lower extremity of wells marked by blue arrows in Fig. 4 whereas drainage was performed by pumping water through the wells marked with red arrows.

(iii) An acoustic source (pendulum) consisting in a stainless steel ball hitting a granite cylinder in contact with the sand. An accelerometer placed on the granite cylinder recorded the source signal: the obtained broad-band spectrum lies in the [0.005–20] kHz frequency range (see Figs 4b and c). This seismic source was designed to generate mainly P waves along the x -axis (Sénéchal *et al.* 2010).

(iv) Nine single component accelerometers (IEPE type, Bruel and Kjaer) with a 50 mV (m s^{-2}) $^{-1}$ sensitivity in the [0–17] kHz range. The accelerometers were aligned with the axis of the granite cylinder and placed in the same direction to obtain a null angle of incidence for the direct P waves (x direction). They were placed every 10 cm, starting from 20 cm to 100 cm from the source. The accelerometers were oriented in order to get a negative polarity first arrival in acceleration $\ddot{\mathbf{U}}$, corresponding to a positive scalar product between wave vector and local displacement \mathbf{U} (see eq. 1).

(v) Eight electric dipoles, composed of two stainless steel electrodes (7 cm long) and their home-made pre-amplifiers (input impedance 1 $\text{G}\Omega$) used for the seismoelectric acquisition. The dipole line (x direction) is in the direction of the accelerometer line but translated by 1 cm laterally (see Fig. 4). The 10-cm-length dipoles were placed every 10 cm from 20 to 90 cm from the source. Since the negative electrode (by convention in our set-up) is located further from the source (the spatial reference) than the positive electrode, the measured difference in electrical potential is $-\Delta V_x$ and $\Delta x = 10$ cm. The seismoelectric field is deduced from this measurement by the relation:

$$E_x = -\frac{\Delta V_x}{\Delta x}. \quad (12)$$

(vi) Six calibrated capacitance probes (Waterscout SM 100 soil moisture sensor from Spectrum technologies) were used to monitor the water saturation S_w in the plane where accelerometers and dipoles were located. The water saturation uncertainty was evaluated to 5 per cent and the S_w value around each accelerometer or dipole was obtained by interpolation of probe measurements using the Inverse Distance Weighting method (Barrière *et al.* 2012). The uniform saturation along the receivers line is shown in Fig. 5).

(vii) Dynamic signal acquisition modules PXI-4498 from National Instruments with 16 simultaneous 24-bit analog inputs per module (316 mV full scale for electrical potential measurements). A 200 kHz sampling rate was used.

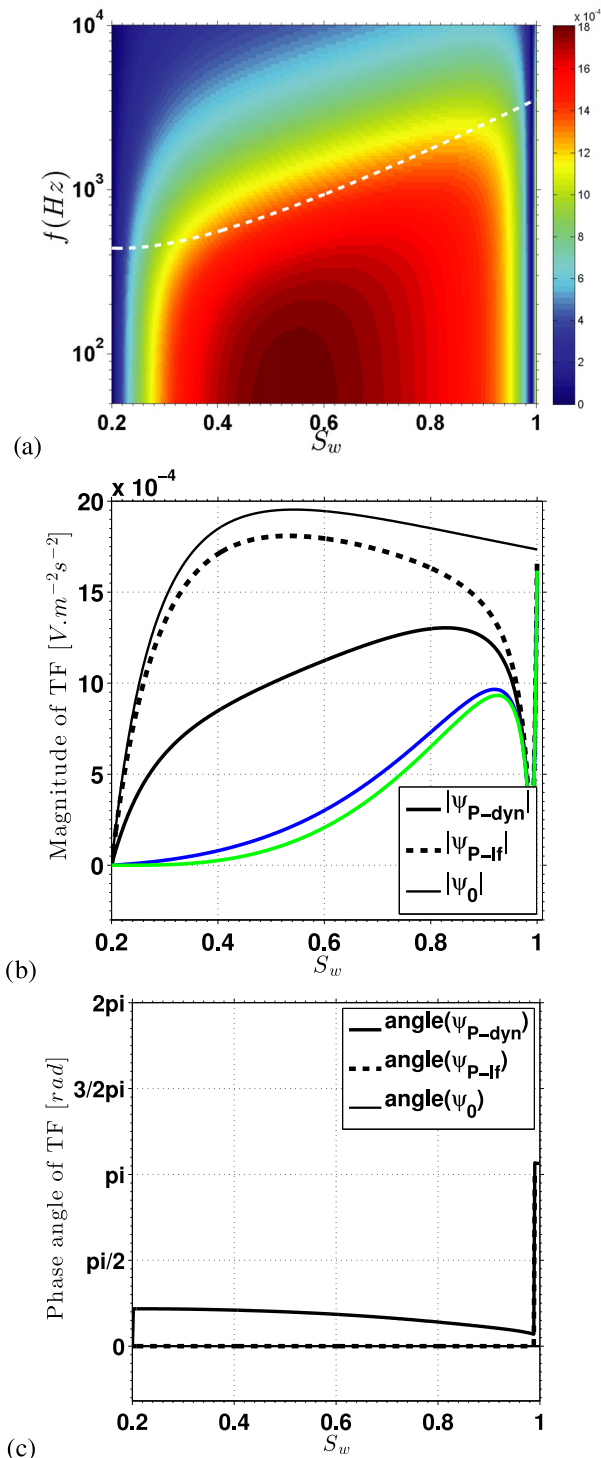


Figure 3. (a) Magnitude of the P -waves dynamic transfer function $|\psi_{P-dyn}(S_w, \omega)|$ as a function of frequency f and saturation S_w , based on the Jackson (2010) model for electrokinetic coupling. The white line gives Biot's frequency values as a function of S_w . (b) and (c): Magnitudes and phase angles as a function of the saturation S_w , respectively for the P -waves dynamic transfer function ψ_{P-dyn} at $f = 1.5$ kHz, for the P -waves low frequency transfer function ψ_{P-lf} and for the P -waves simplified low frequency transfer function ψ_0 in a partially saturated silica sand. Magnitude of dynamic transfer functions obtained with the models of Guichet *et al.* (2003) and Revil *et al.* (2007) are respectively displayed by blue and green curves.

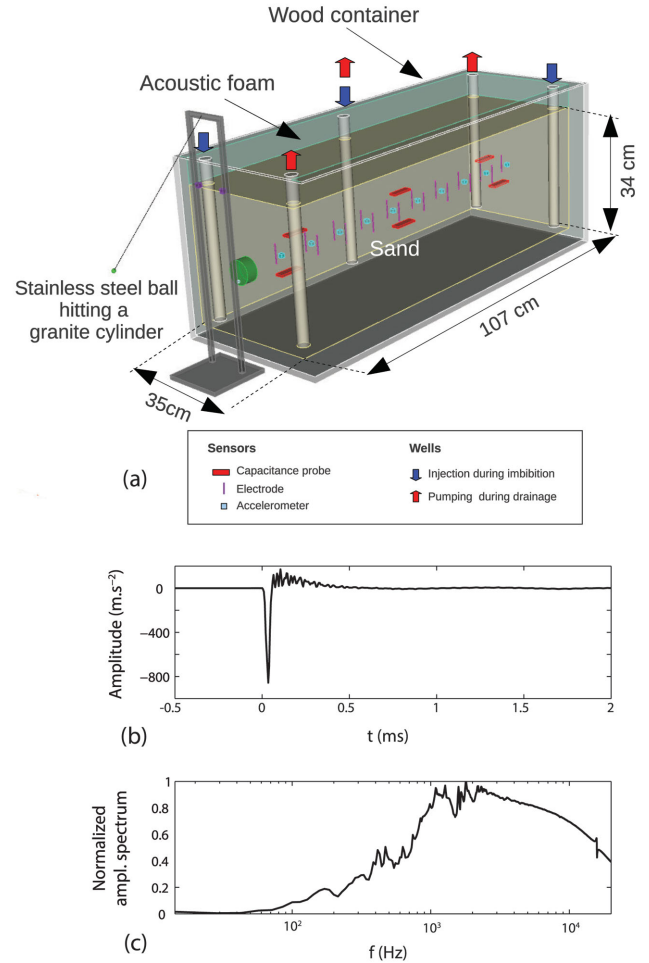


Figure 4. (a) Sketch of the experimental apparatus used in this study. (b) Typical record of the seismic source signal (steel ball hitting the granite) versus time, recorded by an accelerometer located on the granite cylinder. (c) Normalized amplitude spectrum of the source signal shown in (b) as a function of frequency.

3.2 Description of the experimental constraints and parameters

Before starting an experiment, we took care to bring the saturating fluid at electrochemical equilibrium by flowing deionized water through the sand during 48 hr. The water conductivity reached a plateau value around $1.17 \times 10^{-2} \text{ S m}^{-1}$ at 25°C , and the monitoring during the following experiments showed it to be very stable. In this study, we have neglected the surface electrical conductivity (see Appendix A) in particular because it is generally admitted to be lower than $2 \times 10^{-4} \text{ S m}^{-1}$ for silica as long as the water conductivity remains about 10^{-2} S m^{-1} (Glover 1998; Guichet *et al.* 2003).

The oven-dried sand were poured in the container with constant flow by using a large sieve. At the end of the experiment, five cores were extracted from the sample in order to measure their porosity and intrinsic permeability. Permeability was measured by a home made Darcy's apparatus and was estimated to $k_0 = 1.02 \times 10^{-11} \text{ m}^2$. The porosity $\phi = 0.4 \pm 0.02$ was measured by comparing the weight of dried cores to the density of solid grains. Using the Archie's law, we also verified by laboratory measurements that the formation factor $F = \phi/\gamma_0$ is close to 4.3 consistently with the γ_0 value obtained by the formulation of Berryman (1981).

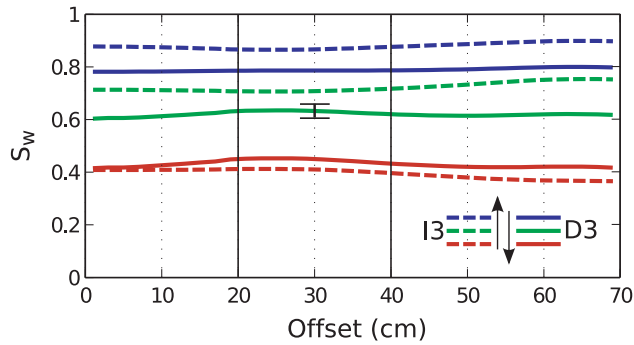


Figure 5. Example of water saturation measurements along the receivers array for different values of S_w . Variations of S_w between offset = 0.2 and 0.4 m are lower than uncertainties on S_w measurements displayed as an example at offset = 0.3 m, during D3, when S_w is close to 0.6.

Injection pressure was obtained by uplifting water containers 40 cm above the tank. Two initial complete cycles were performed to homogenize pore fluid distribution: the first imbibition started from oven-dried sand and was followed by a first drainage and

a second complete cycle. During the last cycle, water saturation variations showed that the saturation could be considered as spatially homogeneous in the horizontal plane of measurements (Fig. 5).

We explored the $S_w = [0.2-0.9]$ range corresponding to respectively the water and gas residual saturations. We performed a time-lapse monitoring while the saturation was varying, by repeating about 25 times (between $S_w = 0.2$ and $S_w = 0.9$) a measurement of an initial saturation measurement followed by 10 seismic/seismoelectric records and a final measurement of the saturation. For each saturation value, the ten seismic and ten seismoelectric records were stacked in order to improve the signal-to-noise ratio.

3.3 Example of measured seismic and seismoelectric data

An example of seismic and seismoelectric data recorded at the beginning of the third drainage ($S_w \approx 0.9$) is presented in Fig. 6 for various offsets. An offset is defined as the distance between the source and the receiver (the accelerometer or the first electrode). It appears from the comparison of Figs 6(c) and (d) that, as expected, seismoelectric data are very sensitive to electromagnetic ambient noise. For each recorded signal, the signal-to-noise ratio (Figs 6e

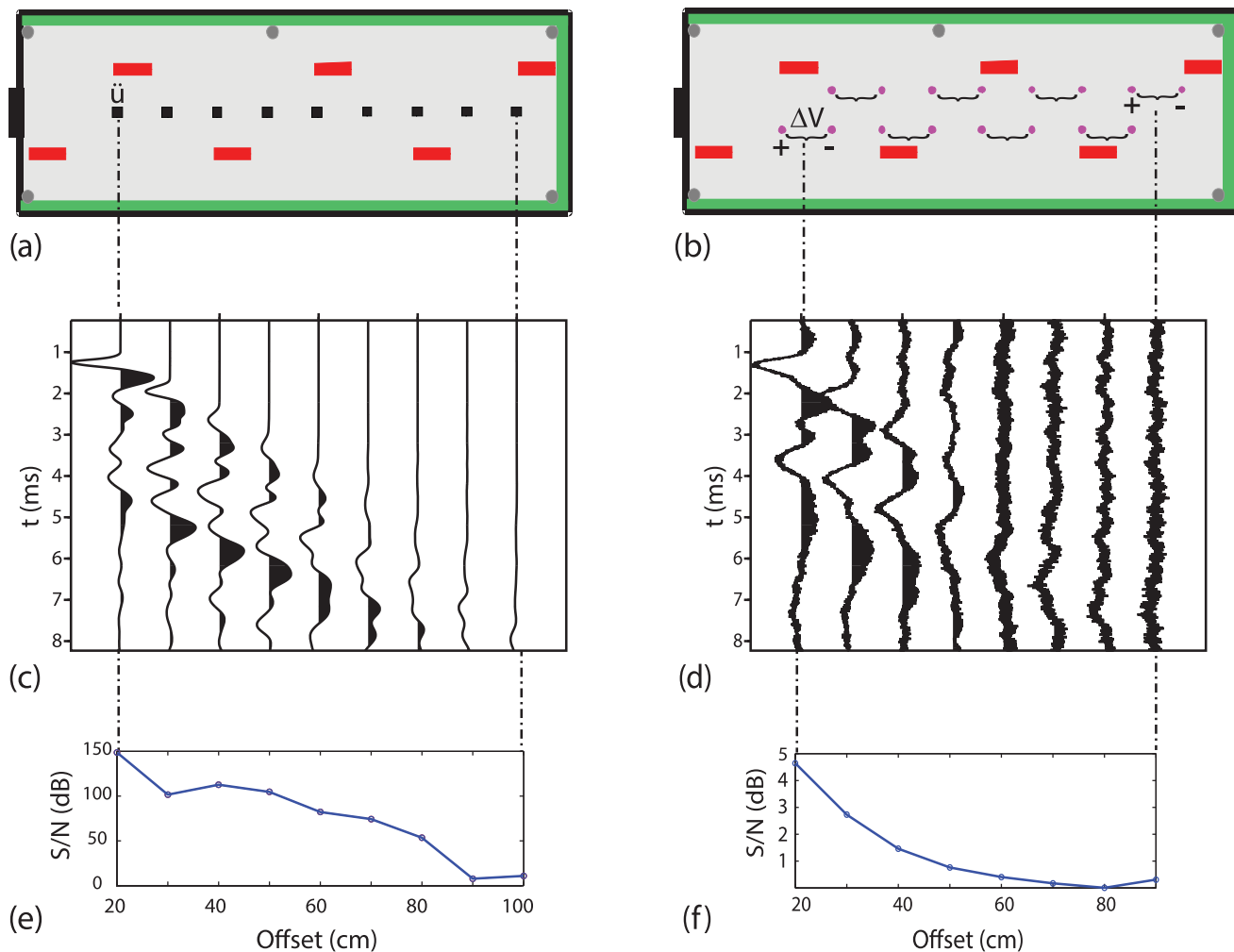


Figure 6. (a) View from above of the horizontal plane of the experimental set-up containing accelerometers (black squares) and capacitance probes (red rectangles). (b) View from above of the same horizontal plane shown in (a) containing dipoles (couple of electrodes in magenta). (c) Seismic records at various offsets (source–receiver distance) obtained at the beginning of the drainage of the third cycle for $S_w \approx 0.9$. (d) Seismoelectric record at various offsets recorded simultaneously to the seismic data shown in (c). (e) Signal-to-noise ratio of the data shown in (c) versus offsets. (f) Signal-to-noise ratio of the data shown in (d) versus offsets.

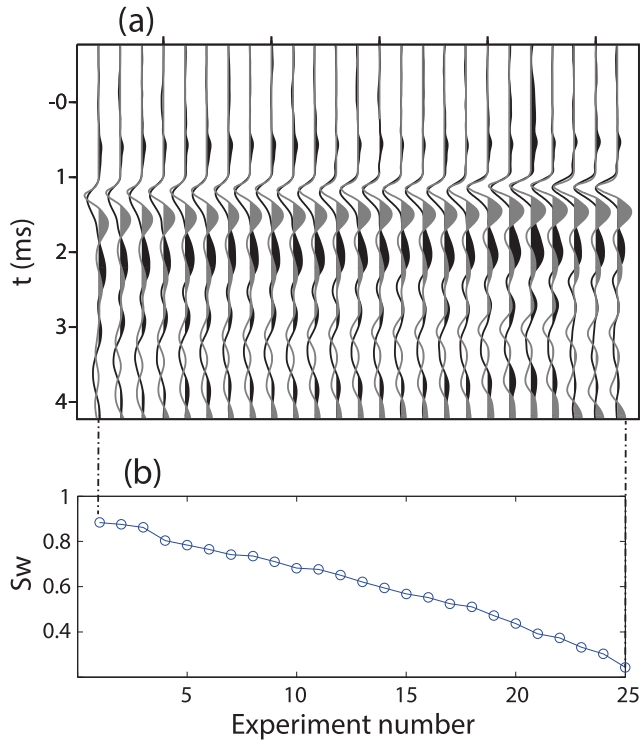


Figure 7. (a) Normalized seismic traces (grey) and seismoelectric fields (black) measured at offset = 0.2 m during the third drainage. (b) S_w coefficient as a function of the experiment number shown in (a).

and f) is computed as $S/N = 10 \log(A_{\text{sig}}/A_{\text{noise}})^2$, the amplitude of the signal A_{sig} being defined as its maximum value during the first 10 ms after triggering, and the noise amplitude A_{noise} being defined as the maximum value of the data before triggering.

All seismic records contain classically different types of seismic waves corresponding to direct, reflected and/or refracted waves. The seismic record in Fig. 6(c) shows fortunately very clear first arrivals up to an offset of 80 cm, with S/N higher than 100 dB as shown in Fig. 6(e). As claimed in Barrière *et al.* (2012), these first seismic arrivals were considered as direct P waves. The very low S/N measured on seismoelectric data (lower than 5 dB in Fig. 6f) implies that waveforms were much more difficult to identify than in seismic signals. The first seismoelectric wave-type signal could indeed be clearly distinguished only on the three first records (offsets 20, 30 and 40 cm) in Fig. 6(d).

We notice in Fig. 6(c) that the first seismic arrivals have a negative polarity consistently with what was expected from the accelerometers specifications (see Section 3.1). The measured coseismic electric field in Fig. 6(d) also presents a first negative signal implying that the corresponding $\mathbf{E}/\dot{\mathbf{U}}$ ratio is positive for the direct P -waves propagating in the partially saturated sand, which is consistent with the theoretical predictions developed in Section 2.3 (see Fig. 3 with a phase angle near zero for ψ_P).

The recorded seismic and seismoelectric signals during the third drainage (S_w decreasing from 0.88 to 0.24) at offset = 20 cm are shown in Fig. 7. In Fig. 7(a), seismic and seismoelectric traces are normalized in order to perform a qualitative comparison of both signals during first arrivals. It appears clearly that the frequency content of seismic and seismoelectric signals are rather different. This observation calls for the use of a time-frequency analysis in order to characterize seismic and seismoelectric attributes. We proceed the data in the following by using a CWT which in turn will

provide amplitudes, frequencies and velocities from the first arrival of seismic and seismoelectric measurements.

4 ANALYSIS OF FIRST SEISMIC AND SEISMOELECTRIC ARRIVALS

We have presented in Section 2 an analytical formulation of the transfer function giving the amplitudes of seismoelectric fields induced by a seismic wave travelling in a porous medium. These transfer functions were given in particular for P and S direct body waves. Barrière *et al.* (2012) performed a 2-D numerical simulation of waves propagation in the present experiment and showed that the first arrivals as shown in Fig. 6(c) were indeed direct P waves, not disturbed by reflected, refracted nor surface waves.

In order to analyse the frequency content of these first P -waves arrivals, we chose to perform a spectral analysis on the first envelope or ‘lobe’ by using a CWT (Daubechies 1992; Mallat & Zhong 1992). This processing is detailed in Section B3. From typical $C(a, b)$ map obtained by CWT, we can extract the following informations concerning the first arrivals:

(i) The main frequency of the first arrival, by picking the scale corresponding to the maximum of $C(a, b)$. The picked scale in Fig. B1(b) was converted in frequency using eq. (B6). The function converting scales into frequencies is shown in Fig. B1(c). The local spectrum can also be estimated from CWT by extracting local maxima in the time window corresponding to the first arrival (highlighted band in Fig. B1b).

(ii) The time at the maximum of $C(a, b)$ in a time window corresponding to the first arrival. From that time we will deduce the propagation time of the first arrival, by subtracting a quarter period corresponding to the main frequency.

(iii) The amplitude of the first arrival by picking the maximum amplitude of the wavelet coefficient in the $C(a, b)$ map.

The CWT using a Mexican hat wavelet, shown as an example here, was performed on all seismic and seismoelectric data sets. We focus in the following on the results of cycle 3 (imbibition and drainage written respectively, I3 and D3).

4.1 Seismic and seismoelectric velocities

The apparent velocity of seismic and seismoelectric fields are deduced from the analysis of $C(a, b)$ maps. We picked the main frequency (see Section 4.2) and the corresponding time for all measurements, and then subtracted to that picked time a quarter period at the main frequency in order to get a precise estimation of the absolute ‘first break’ time. For a given experiment, this time determination is performed for all offsets. The apparent velocity for seismic and seismoelectric data is then deduced by a linear regression of all these first break times versus distances. Only the first three positions (offsets) were used since the seismoelectric data became too noisy after offset 0.4 m. We found that the described apparent velocity determination technique was well suited for seismoelectric measurements which first breaks were not always very clear in the raw data (see for example Fig. 6e).

A compilation of seismic and seismoelectric apparent velocities measured during the third cycle is shown in Fig. 8 as a function of saturation S_w . At first order, a rather constant mean apparent velocity for seismic and seismoelectric fields was found lower than 200 m s^{-1} (between 140 and 180 m s^{-1}) during both drainage and imbibition. Nearly identical velocities in seismic and in

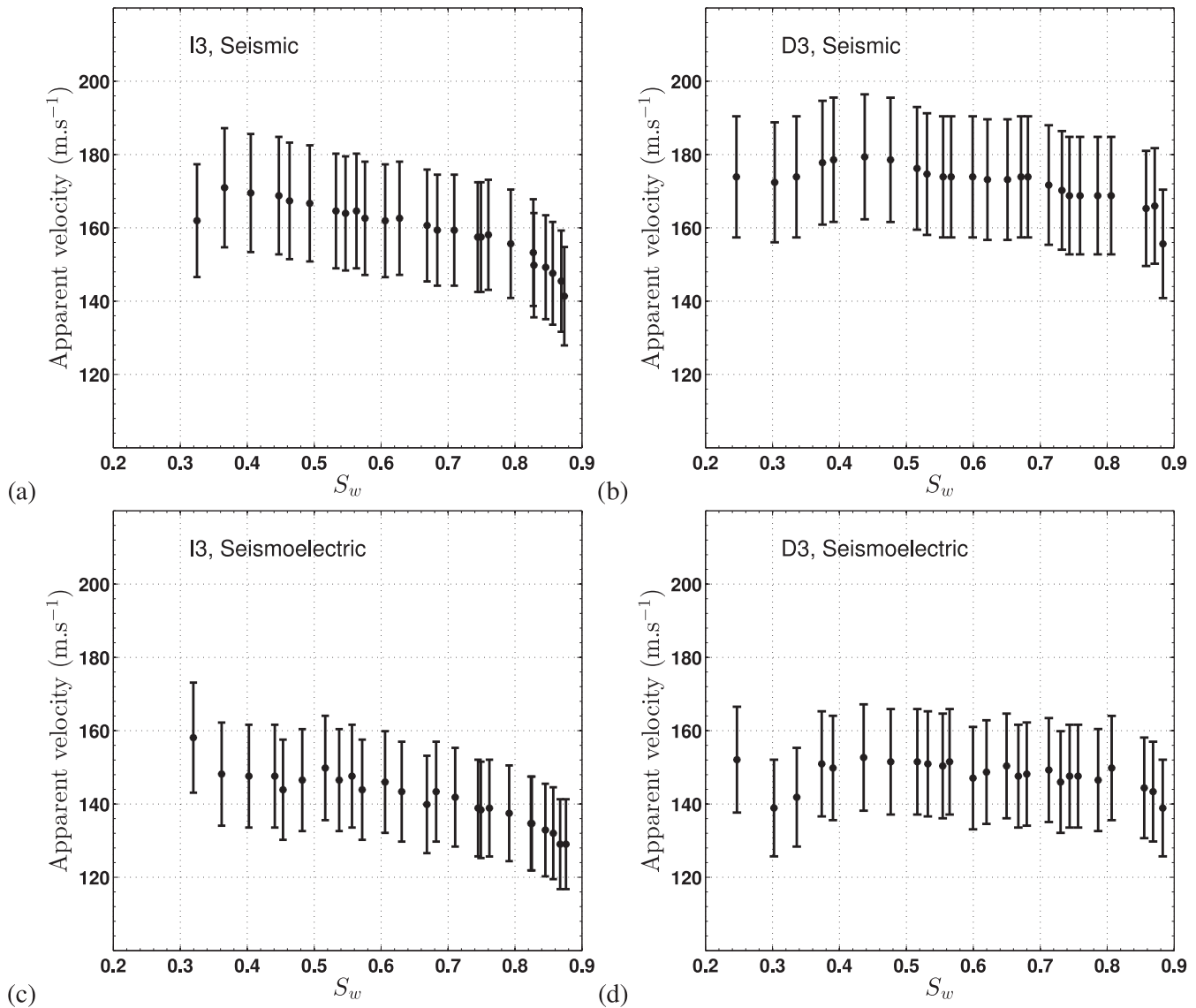


Figure 8. Apparent seismic and seismoelectric velocities measured during the third cycle as a function of S_w . (a), (b), (c) and (d) are respectively the seismic velocities during imbibition (I3), seismic velocities during drainage (D3), seismoelectric velocities during imbibition and seismoelectric velocities during drainage. The error bars, around 10 per cent of the measured velocity, originate from uncertainties on the accelerometers locations (± 5 mm), on the picking times ($\pm 4 \times 10^{-5}$ s) and on the dipole lengths between coupled electrodes (± 10 mm).

seismoelectric demonstrates the expected coseismic origin of the seismoelectric data measured experimentally.

Barrière *et al.* (2012) monitored the phase velocity during imbibition and drainage also in the CWT domain by using a complex ‘Morlet’ instead of a real ‘Mexican hat’ wavelet used in this study. The method consisted in picking time shifts both in amplitude and in phase spectra, and in deducing the corresponding phase velocity. Here, our simplified procedure using a real ‘Mexican hat’ wavelet, chosen because it appears the more adapted to describe the studied first lobe of the signal, gave results comparable to those of Barrière *et al.* (2012) in terms of velocity values of the direct P waves.

4.2 Frequency content of seismic and seismoelectric fields

Main frequencies obtained by CWT in seismic and seismoelectric data during the third cycle are presented in Fig. 9. The first obser-

vation is that main frequencies globally decrease as a function of an increasing offset, either in seismic or in seismoelectric fields: that is understood as a classic attenuation effect of the higher frequencies. A second common characteristic in seismic and seismoelectric frequencies (Figs 9a–d) is a decrease of frequencies as a function of an increasing water saturation S_w . That trend, already observed by Barrière (2011) in a purely seismic context, was attributed to Biot’s losses attenuation combined to effective permeability effects.

It appears systematically in Fig. 9 that for a given water saturation, the main frequency of the first seismic lobe is higher than the counterpart seismoelectric first lobe frequency; seismic frequencies remain for example always about twice higher than the seismoelectric frequencies at offset 0.2 m. These gaps in frequency cannot be explained by the low frequency transfer functions (ψ_0 and ψ_{P-1f}) since the latter assume that seismic and seismoelectric signals are linearly dependent in time and frequency (see eq. A8 in Appendix A). In other words, the low frequency transfer function

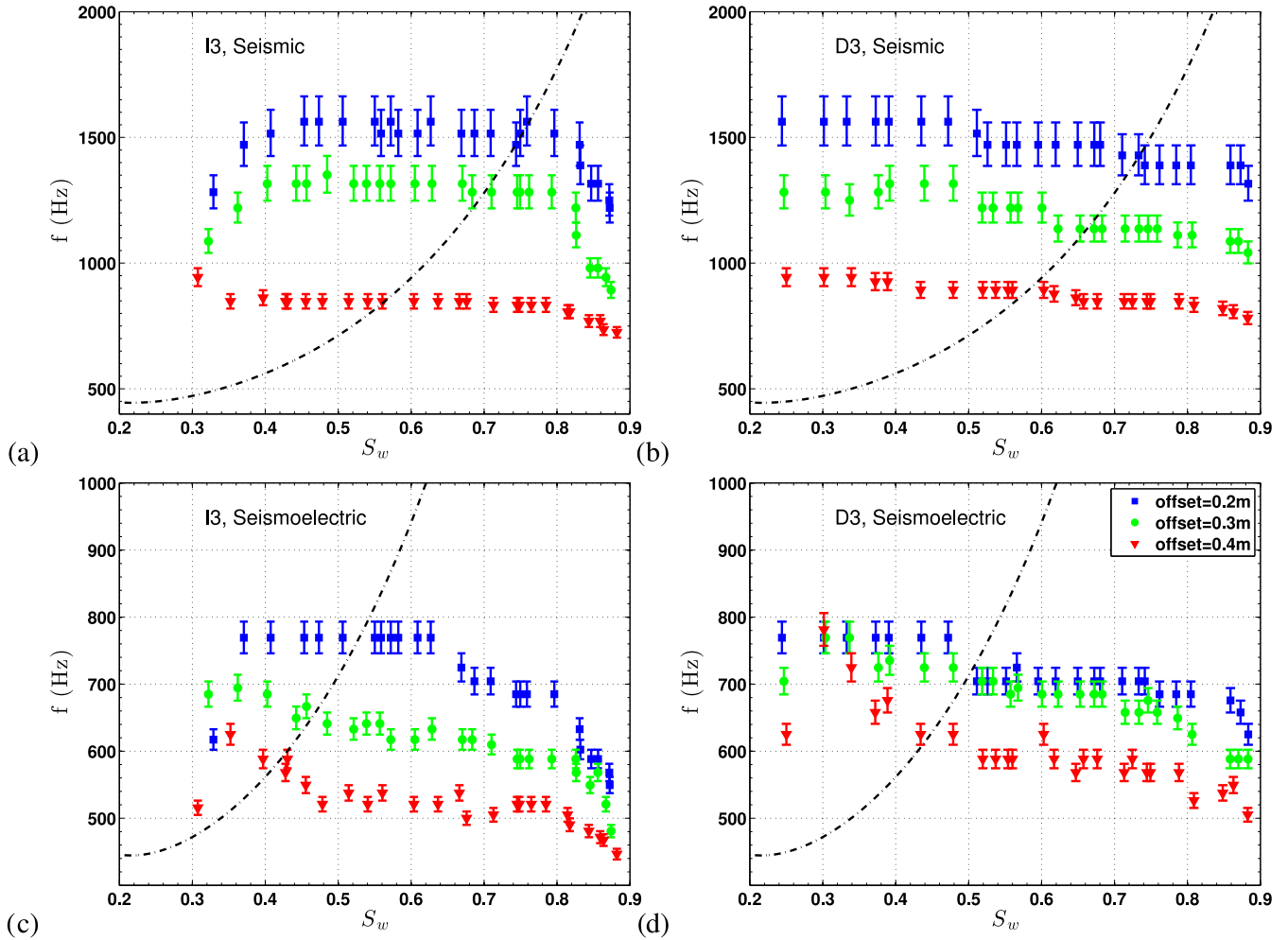


Figure 9. Main frequency (picked from a CWT signal processing) obtained during the third cycle from respectively (a) the seismic data during imbibition, (b) the seismic data during drainage, (c) the seismoelectric data during imbibition and (d) seismoelectric data during drainage. All figures are shown as a function of the saturation S_w and for three different offsets: blue squares 0.2 m, green circles 0.3 m and red triangles 0.4 m. The error bars originate from uncertainties in picking pseudo frequencies (± 2 samples around the maximum amplitude). The variations in Biot's frequency versus saturation (computed from eq. 5 and Appendix A) during those experiments are shown with a dashed black line.

derived from Pride's model extended to the effective fluid presented in Section 2.2 can not account for all the seismic and seismoelectric main frequencies discrepancies observed in Fig. 9, especially when the measured frequency is lower than the Biot's frequency (correspond in Fig. 9 to $S_w \gtrsim 0.6$). Some data in Fig. 9 are well above the Biot's frequency and dynamic effect are probably coming into play in the transfer function between seismic and seismoelectric fields. At least qualitatively, we may infer from Fig. 9 that the frequency content would be modified when the measured frequency crosses the Biot's frequency, corresponding to changes in attenuation mechanisms (inertial or viscous flows).

Computations performed in Section 2.2 showed that we expect a decrease of the magnitude of the ratio $|\mathbf{E}/\dot{\mathbf{U}}|$ as a function of the frequency, for a given S_w , when the main seismic frequency exceeds the Biot's frequency (follow a vertical direction in Fig. 3a for a given S_w). More precisely, we estimate from these computations that $|\psi_{P-dyn}(0.6 \text{ kHz})|/|\psi_{P-1f}| \simeq 0.85$ when $|\psi_{P-dyn}(1.5 \text{ kHz})|/|\psi_{P-1f}| \simeq 0.55$ for $S_w = 0.6$: we then expect experimentally the magnitude of the transfer function $|\psi_{P-dyn}|$ to decrease for f above the Biot's frequency (at a given S_w), meaning that the seismic amplitudes at a given frequency should decrease less rapidly than the seismoelectric

amplitudes at that same frequency. We can not conclude in Fig. 9 if this trend is observed since only the main frequencies are shown and that seismic and seismoelectric main frequencies do not overlap; we will discuss this point further in Section 4.3.

The strong difference in dominating frequency between seismic and seismoelectric signals mentioned above is a quite common observation in laboratory measurements (Zhu & Toksöz 2003; Bordes *et al.* 2006, 2008) as well as in seismoelectric surveys, even at seismic frequencies much lower than the Biot's frequency (Strahser *et al.* 2007; Dupuis *et al.* 2009). Since large dipoles are strongly disturbed by electromagnetic noise, authors generally try to reach a compromise by improving the signal-to-noise ratio (Garambois 1999). Some preliminary tests showed in our case that a 10 cm dipole length was a suitable distance between electrodes, giving satisfying signal-to-noise ratio. Nevertheless, seismic signals, obtained with a calibrated and localized sensor, can be directly interpreted as local acceleration whereas seismoelectric measurements are indirect since they are obtained by a dipole. To our knowledge, the role of the acquisition geometry was never discussed so far, and we suspect that the dipole length might have an effect on the frequency content of the seismoelectric signal. A better understanding of the frequency

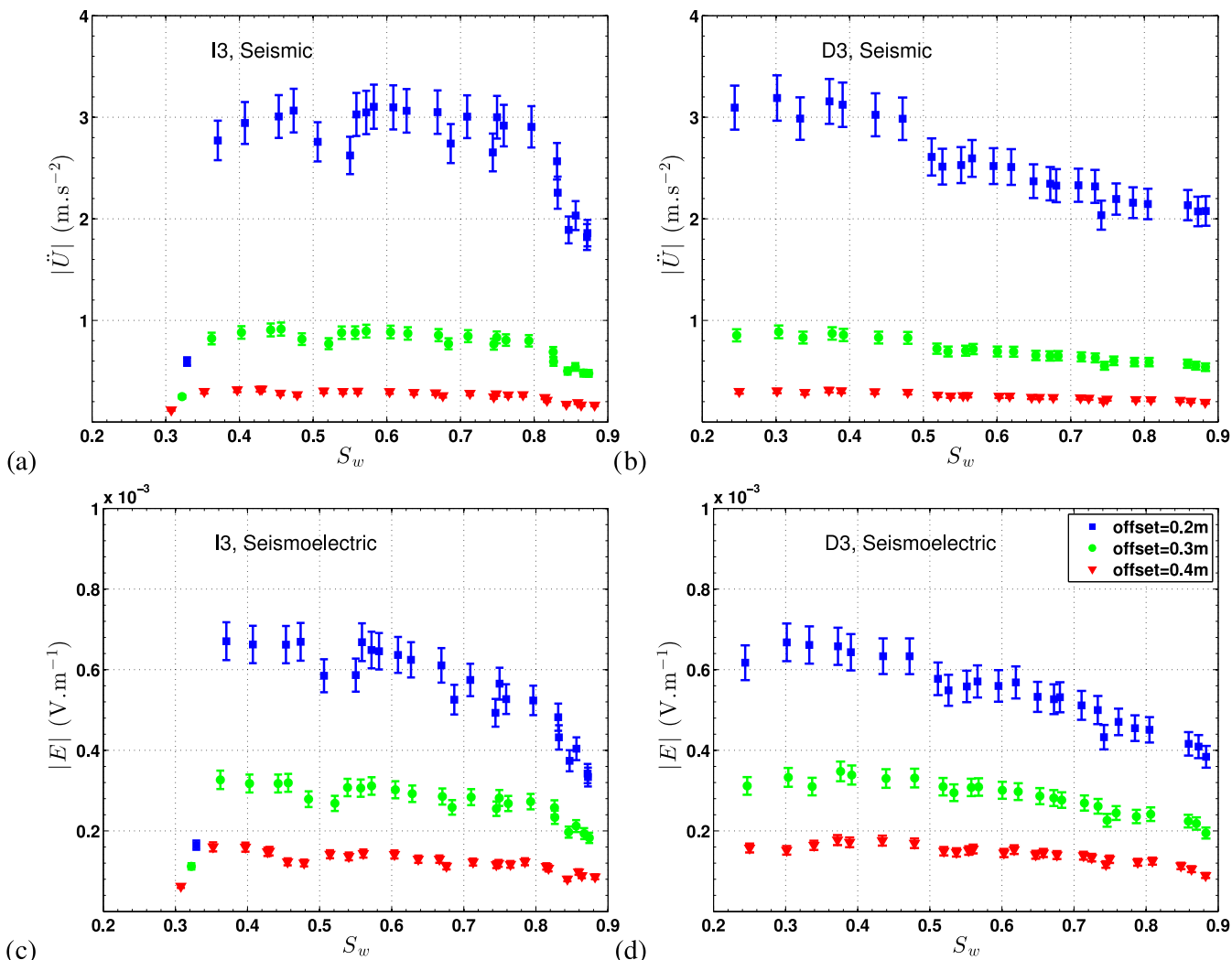


Figure 10. First arrival amplitude (picked in time signals) during the third cycle from, respectively (a) the seismic data during imbibition, (b) the seismic data during drainage, (c) the seismoelectric data during imbibition and (d) seismoelectric data during drainage. All figures are shown as a function of the saturation S_w and for three different offsets: blue squares 0.2 m, green circles 0.3 m and red triangles 0.4 m. The associated error bars (around 7 per cent) in seismic and seismoelectric amplitudes originate from uncertainties in the receivers location (± 5 mm), in the dipole length (± 10 mm) and on the picking of the maximum amplitude (± 2 samples around the maximum amplitude).

mismatch between seismic and seismoelectric would require a more complete experimental and/or numerical study addressing the effect of acquisition geometry on seismoelectric frequency content which was not our initial purpose.

4.3 Amplitudes ratios

The maximum amplitude of the first arrival in seismic and seismoelectric experiments during cycle 3 are shown in Fig. 10. These amplitudes were directly extracted from the signal in time by picking the maximum of the first lobe. As expected, measured amplitudes decrease as a function of offset and decrease also as a function of water saturation in the range $S_w = [0.2-0.9]$, consistently with previous observations of Parkhomenko & Tsze-San (1964) for seismoelectric measurements and Barrière *et al.* (2012) for seismic measurements. These absolute amplitudes can not be however directly interpreted in term of seismoelectric coupling since, for example, the seismic amplitudes strongly depend on seismic attenuation. That is why the transfer functions built upon a ratio of a coseismic

to a seismic field, can precisely be seen as a direct measurement of seismoelectric coupling.

In order to derive experimental transfer functions from our data, we start with a ‘static’ approach consisting in directly computing the ratio of the seismoelectric to seismic maximum amplitudes: this procedure assumes that the transfer function does not depend on frequency although measured seismic and seismoelectric main frequencies are significantly different (see Section 4.2). These ratio $|\mathbf{E}/\dot{\mathbf{U}}|_{\text{exp}}$ are presented in Fig. 11 for the experiments performed during the third cycle. We have obtained these ratio by two independent ways: the first technique called ‘Time-static’ in Figs 11(a) and (b) is obtained from the data picked in time signals (shown in Fig. 10). The second technique, labelled ‘CWT-static’ in Figs 11(b) and (d), consists in picking the amplitudes of the first arrival (respectively in seismoelectric and in seismic signals) associated to the main frequency obtained by CWT (see Section 4.2) and then perform the ratio.

The two independent techniques of measurement of $|\mathbf{E}/\dot{\mathbf{U}}|_{\text{exp}}$ lead to the same conclusion: the ratio of seismoelectric to seismic

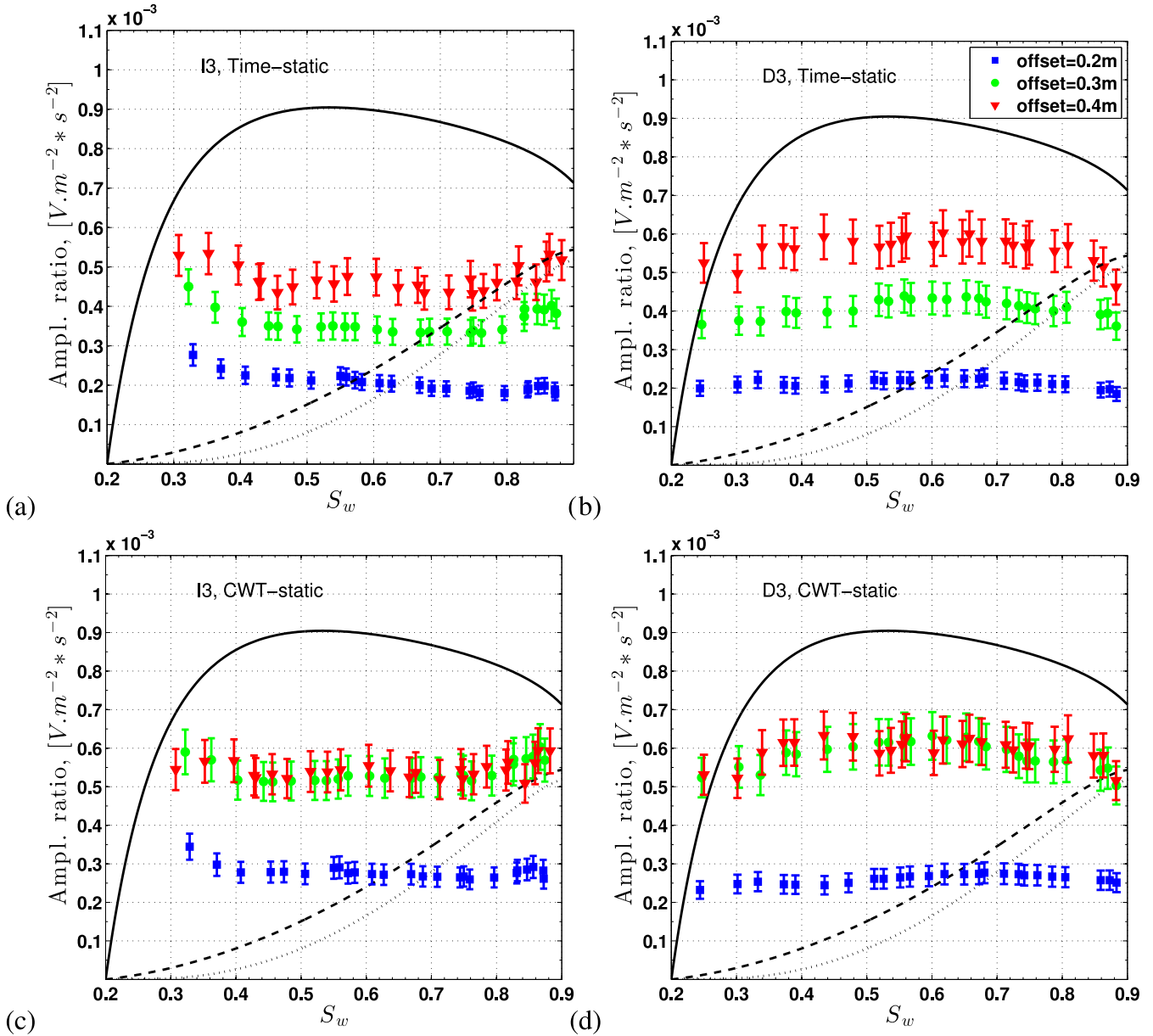


Figure 11. Amplitude ratios of seismoelectric to seismic field as a function of S_w measured during the imbibition of the third cycle in (a) and (c), and during the drainage of the third cycle in (b) and (d) at offset = 0.2 m (blue squares), at offset = 0.3 m (green circles) and offset = 0.4 m (red triangles). The amplitude ratios obtained in the ‘static approach’ are obtained in (a) and (b) by picking the maximum amplitude in time signals (Time-static), and in (c) and (d) by picking maximum amplitudes of seismic and seismoelectric first arrival in the C(a,b) map. The low frequency transfer function $|\psi_{P-1f}(S_w)|$ predictions are obtained by applying an electrokinetic coefficient two times smaller compared to the theoretical C_{ek} computed in Appendix A. They are superimposed in Fig. (a) and (b) using the model of Jackson (2010) in solid line, Guichet *et al.* (2003) long dashed line and Revil *et al.* (2007) short dashed line.

signals is at first order constant as function of the saturation S_w for a given offset in the explored range $S_w = [0.2-0.9]$. In terms of order of magnitude, the mean $|\mathbf{E}/\dot{\mathbf{U}}|_{\text{exp}}$ is about $4 \times 10^{-4} \pm 25$ per cent. Although the two techniques are rather different, one processing the data in the time domain and the other one in the CWT, the differences in the ratios remain as small as $\sim 10-25$ per cent (comparison of Fig. 10a with Fig. 11c, and Fig. 11 with Fig. 11d).

These results can also be compared to the theoretical transfer function discussed in Section 2.3. The continuous and dashed lines in Fig. 11 are obtained by computing the $|\psi_{P-1f}(S_w)|$ with the three electrokinetics models presented in Table 2. Nevertheless, the models are computed by considering an electrokinetic coefficient

two times smaller compared to the theoretical C_{ek} computed in Appendix A, which were based on the $C_{ek}(S_w) = 1$ values measured by Guichet *et al.* (2003) [here we use $C_{ek}(S_w = 1)/2$]. It appears from Fig. 11 that amplitude ratios as a function of the saturation are well reproduced by the capillary tubes model of Jackson (2010) (plateau) whereas the increase predicted by Guichet *et al.* (2003) and Revil *et al.* (2007) is not retrieved in the data.

The comparison of an ‘experimental transfer function’ with the dynamical transfer functions predictions seen in Section 2 would require to perform spectra ratios on a broad-band frequency range; the analysis of both amplitude and phase of spectra ratios could lead to a discussion on the validity of the dynamic transfer function.

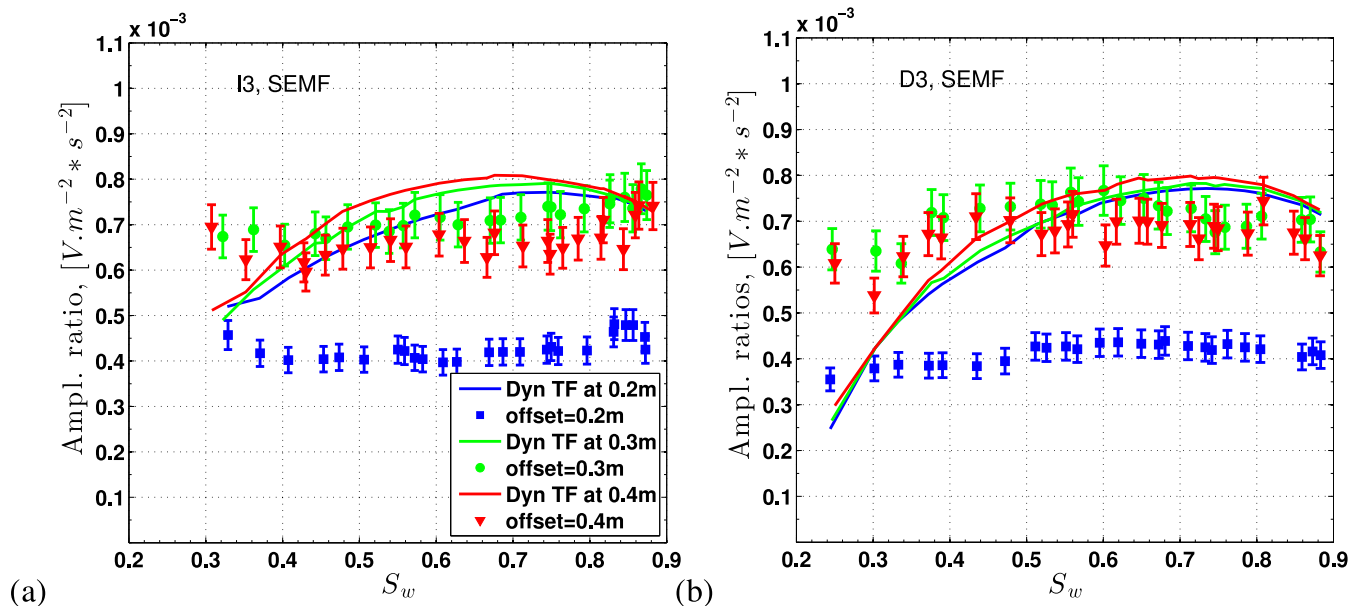


Figure 12. Amplitude ratios of seismoelectric to seismic field as a function of S_w measured during the imbibition (a) and drainage (b) of the third cycle. These data are obtained with the ‘dynamic approach’ by picking the maximum amplitude at the main frequency of seismoelectric data, and, thereafter, by picking the counterpart seismic amplitude at that same seismoelectric main frequency (denoted SEMF, ‘SeismoElectric Main Frequency’) in local maxima curve of the $C(a, b)$ maps. Dynamic transfer functions are also computed at the observed frequency for each offset, using the Jackson (2010) model with an electrokinetic coefficient two times smaller compared to the theoretical C_{ek} computed in Appendix A.

Unfortunately, in the present experiment, the explored frequency range is too narrow and such a complete analysis is out of reach. An alternative approach consists in calculating amplitude ratios extracted from the $C(a, b)$ maps at the main frequency or at a frequency in the vicinity of the main frequency. The ‘dynamic’ approach consists in picking the maximum amplitude at the main frequency in seismoelectric data (shown in Figs 10c and d), and, thereafter, in picking the counterpart seismic amplitude at that same seismoelectric main frequency (denoted SEMF, ‘SeismoElectric Main Frequency’) in the $C(a, b)$ maps. We then perform the ratio between those amplitudes for all experiments at various saturation and obtain the results in Fig. 12. Similarly to the ‘static’ approach shown in Fig. 11, it results that those ratios, for a given offset, are nearly constant as a function of saturation with a mean value $5 \times 10^{-4} \pm 25$ per cent. The data in Fig. 12 can be compared to the theoretical prediction of the dynamical transfer function $|\psi_{P-dyn}(S_w)|$ using the Jackson (2010) model with an electrokinetic coefficient equal to $C_{ek}(S_w = 1)/2$. Since the working frequencies in the experiments are close to the Biot’s frequency, as discussed in Section 2.3, the theoretical dynamical transfer functions are significantly different in amplitudes compared to static ones: the dynamic transfer functions are closer to the data than the static ones.

Our ‘static’ and ‘dynamic’ approaches of the experimental data demonstrate that for given offset, the ratio $|\mathbf{E}/\ddot{\mathbf{U}}|_{exp}$ remain nearly constant during the experiments even if the range of variation $S_w = [0.2-0.9]$ is quite large. This global trend is particularly well recovered by the Jackson’s model (2010) coupled to the extended theory of Pride (1994) to a partially saturated fluid. More quantitatively, there is however a mismatch in terms of amplitude of the ratio $|\mathbf{E}/\ddot{\mathbf{U}}|$: the theoretical predictions are systematically much lower than the experimental data, about a factor 4 when the static approach is used and about a factor 2 when the dynamic approach is used. This mismatch could originate from an overestimation of electrokinetic coefficient C_{ek} (see Appendix B) or from our choice

of dipole length. Indeed, we observe that the dipole length can modify the amplitude of the measured E field by a coefficient ranging 1.5–4, but not depending on the saturation.

5 CONCLUSION

Pride & Haartsen (1996) wrote the expressions of transfer functions from seismic to seismoelectric fields in a saturated porous medium. Later, Garambois & Dietrich (2001) proposed a simplified low frequency transfer function applicable when seismic frequencies are below Biot’s frequency. Both studies were performed in a saturated porous media. We have generalized the transfer functions formulations to a partially saturated porous medium and have consequently derived analytical expressions of dynamic and low frequency transfer functions for P and S waves, respectively $\psi_{P-dyn}(S_w, \omega)$, $\psi_{P-1f}(S_w)$ and $\psi_{S-dyn}(S_w, \omega)$, $\psi_{S-1f}(S_w, \omega)$. The generalization to partially saturated medium was done using an effective fluid model under various hypotheses; we have in particular neglected the surface conductivities and used characteristic models of variations of the electrokinetic coupling C_{ek} as a function of the partial saturation S_w . In this study, we have particularly emphasized the model proposed by Jackson (2010). The effective fluid model also assumes that the seismic wavelengths are larger than the fluid heterogeneities.

The theoretical P -waves transfer functions showed significant variations in magnitude versus saturation and versus frequency. For a given frequency, the magnitude $|\psi_{P-dyn}(S_w)|$ increases in the typical range $S_w = [0.2-0.4]$ but is predicted to be nearly constant in the $S_w = [0.4-0.9]$ range. For a given saturation, $|\psi_{P-dyn}(f)|$ versus frequency is firstly constant before rapidly decreasing once we exceed Biot’s frequency. The variation of $|\psi_{P-dyn}(S_w, \omega)|$ is of the order 10 in the considered range ($S_w = [0.2-0.9]$, $f = [10-10^4]$ Hz) and depends both on the used model for $C_{ek}(S_w)$ and on the chosen frequency. We have also shown numerically that the magnitude of the P -waves

low frequency transfer functions follows closely the dynamic one when $f \leq f_c$. We also showed that the low frequency transfer function may be carefully simplified in partially saturated media since excessive simplification introduces errors on phase predictions at highest saturations. Finally, we confirmed that the transfer function of the shear S waves is tiny compared to the P -waves case; we concluded that the S -waves transfer functions may not be used either in experimental or numerical conditions.

We have then compared our theoretical predictions to data recorded in a partially saturated tank of silica sand: S_w was monitored during experiments (drainage and imbibition), the seismic field was recorded using accelerometers while the seismoelectric field was recorded using a couple of electrodes at mid-height of the 1-m-length-scale container. We have shown using the CWT that the seismic field had systematically a main frequency about twice as big as the main seismoelectric frequency; that observation was true for all offsets (distance to the source).

We have also estimated the experimental ratios $|\mathbf{E}_P(S_w)/\ddot{\mathbf{U}}_P(S_w)|$ with various methods (picking in time and CWT) and those ratios appear to be approximatively constant during the experiments in the range $S_w = [0.2-0.9]$ for all offsets. The comparison of data with the theory led to the conclusion that the trend and the order of magnitude of the recorded experimental transfer functions is recovered by the theoretical prediction when using the Jackson (2010) model for the saturation dependence of electrokinetic coefficient. Working near the Biot's frequency in the experiments, we verified that dynamics effects come into play since the dynamic transfer function is closer to the data than the static transfer function. We have also demonstrated that the CWT processing is well suited for estimating apparent velocities, main frequencies and amplitude ratio at the main frequency of the data.

This study confirms that introducing the effective fluid model into the Pride's theory is appropriate when wavelengths are larger than the fluid heterogeneities. Nevertheless, the accuracy of the predicted transfer function strongly depends on electrokinetic models, that have to be completed to account more precisely for the fluid distribution that can involve different fluid thicknesses with strong effects on the effective viscosity and permeability.

ACKNOWLEDGEMENTS

This study has benefited to the ANR program of the French government, especially via the TRANSEK project. The authors thanks S. Garambois, G. Sénéchal and D. Rousset for their constructive suggestions and J. Holzhauser for reading carefully the original manuscript.

REFERENCES

- Allègre, V., Jouniaux, L., Lehmann, F. & Sailhac, P., 2010. Streaming potential dependence on water-content in fontainebleau sand, *Geophys. J. Int.*, **182**(3), 1248–1266.
- Allègre, V., Lehmann, F., Ackerer, P., Jouniaux, L. & Sailhac, P., 2012. A 1-D modelling of streaming potential dependence on water content during drainage experiment in sand, *Geophys. J. Int.*, **189**(1), 285–295.
- Archie, G.E., 1942. The electrical resistivity log as an aid in determining some reservoir characteristics, *Trans. Am. Inst. Min. Metall. Pet. Eng.*, **146**, 54–62.
- Bachrach, R. & Nur, A., 1998. High-resolution shallow-seismic experiments in sand. Part I: water table, fluid flow, and saturation, *Geophysics*, **63**(4), 1225–1233.
- Bachrach, R., Dvorkin, J. & Nur, A., 1998. High-resolution shallow-seismic experiments in sand. Part II: velocities in shallow unconsolidated sand, *Geophysics*, **63**(4), 1234–1240.
- Barriere, J., 2011. Atténuation et dispersion des ondes P en milieu poreux partiellement saturé: une approche expérimentale, *PhD thesis*, Université de Pau et des Pays de l'Adour, France.
- Barrière, J., Bordes, C., Brito, D., Sénéchal, P. & Perroud, H., 2012. Laboratory monitoring of P waves in partially saturated sand, *Geophys. J. Int.*, **191**(3), 1152–1170.
- Berryman, J.G., 1981. Elastic wave propagation in fluid-saturated porous media, *Acoust. Soc. Am. J.*, **69**, 416–424.
- Biot, M.A., 1956a. Theory of propagation of elastic waves in a fluid-saturated porous solid: I. low frequency range, *J. acoust. Soc. Am.*, **28**(2), 168–178.
- Biot, M.A., 1956b. Theory of propagation of elastic waves in a fluid-saturated porous solid: II. high frequency range, *J. acoust. Soc. Am.*, **28**(2), 178–191.
- Biot, M.A., 1962. Mechanics of deformation and acoustic propagation in porous media, *J. appl. Phys.*, **34**(1), 36–40.
- Block, G.I. & Harris, J.G., 2006. Conductivity dependence of seismoelectric wave phenomena in fluid-saturated sediments, *J. geophys. Res.: Solid Earth (1978–2012)*, **111**(B1), doi:10.1029/2005JB003798.
- Bordes, C., Jouniaux, L., Dietrich, M., Pozzi, J.-P. & Garambois, S., 2006. First laboratory measurements of seismo-magnetic conversions in fluid-filled Fontainebleau sand, *Geophys. Res. Lett.*, **33**(1), doi:10.1029/2005GL024582.
- Bordes, C., Jouniaux, L., Garambois, S., Dietrich, M., Pozzi, J.-P. & Gaffet, S., 2008. Evidence of the theoretically predicted seismo-magnetic conversion, *Geophys. J. Int.*, **174**(2), 489–504.
- Butler, K.E. & Russell, R.D., 1993. Subtraction of powerline harmonics from geophysical records, *Geophysics*, **58**(6), 898–903.
- Carcione, J.M., 2001. *Wave Fields in Real Media : Wave Propagation in Anelastic, Anisotropic and Porous Media*, Pergamon, Elsevier Science Ltd.
- Chen, B. & Mu, Y., 2005. Experimental studies of seismoelectric effects in fluid-saturated porous media, *J. Geophys. Eng.*, **2**(3), 222–230.
- Darnet, M. & Marquis, G., 2004. Modelling streaming potential (sp) signals induced by water movement in the vadose zone, *J. Hydrol.*, **285**(1), 114–124.
- Daubechies, I., 1992. Ten lectures on wavelets, in *Proceedings of the CBMS NSF Regional Conference Series in Applied Mathematics*, SIAM, Philadelphia.
- Doussan, C. & Ruy, S., 2009. Prediction of unsaturated soil hydraulic conductivity with electrical conductivity, *Water Resour. Res.*, **45**(10), doi:10.1029/2008WR007309.
- Dukhin, A., Goetz, P. & Thommes, M., 2010. Seismoelectric effect: a non-isochoric streaming current. 1. Experiment, *J. Coll. Interface Sci.*, **345**(2), 547–553.
- Dupuis, J., Butler, K., Kepic, A. & Harris, B., 2009. Anatomy of a seismoelectric conversion: measurements and conceptual modeling in boreholes penetrating a sandy aquifer, *J. geophys. Res.*, **114**(B10), B10306, doi:10.1029/2008JB005939.
- Dupuis, J.C. & Butler, K.E., 2006. Vertical seismoelectric profiling in a borehole penetrating glaciofluvial sediments, *Geophys. Res. Lett.*, **33**(16), doi:10.1029/2006GL026385.
- Dupuis, J.C., Butler, K.E. & Kepic, A.W., 2007. Seismoelectric imaging of the vadose zone of a sand aquifer, *Geophysics*, **72**, A81–A85.
- Frenkel, J., 1944. On the theory of seismic and electroseismic phenomena in a moist soil, *J. Phys.*, **8**(4), 230–241.
- Garambois, S., 1999. Etudes expérimentales et théoriques des conversions d'ondes sismo-électriques dans les milieux poreux superficiels, *PhD thesis*, Université Joseph Fourier, Grenoble 1.
- Garambois, S. & Dietrich, M., 2001. Seismoelectric wave conversions in porous media: field measurements and transfer function analysis, *Geophysics*, **66**(5), 1417–1430.
- Garambois, S. & Dietrich, M., 2002. Full waveform numerical simulations of seismoelectromagnetic wave conversions in fluid-saturated stratified porous media, *J. geophys. Res.*, **107**(B7), ESE 5-1–ESE 5-18.

- Glover, P., 1998. Nature of surface electrical conductivity sandstones, and clays, *Geophys. Res. Lett.*, **25**(5), 691–694.
- Guan, W. & Hu, H., 2008. Finite-difference modeling of the electroseismic logging in a fluid-saturated porous formation, *J. Comput. Phys.*, **227**(11), 5633–5648.
- Guichet, X., Jouniaux, L. & Pozzi, J.-P., 2003. Streaming potential of a sand column in partial saturation conditions, *J. geophys. Res.*, **108**(B3), 1248–1266.
- Guichet, X., Jouniaux, L. & Catel, N., 2006. Modification of streaming potential by precipitation of calcite in a sand–water system: laboratory measurements in the pH range from 4 to 12, *Geophys. J. Int.*, **166**, 445–460.
- Haines, S.S., Guitton, A. & Biondi, B., 2007a. Seismoelectric data processing for surface surveys of shallow targets, *Geophysics*, **72**, G1–G8.
- Haines, S.S., Pride, S.R., Klemperer, S.L. & Biondi, B., 2007b. Seismoelectric imaging of shallow targets, *Geophysics*, **72**, G9–G20.
- Jackson, M., 2010. Multiphase electrokinetic coupling: insights into the impact of fluid and charge distribution at the pore scale from a bundle of capillary tubes model, *J. geophys. Res.*, **115**(B7), B07206, doi:10.1029/2009JB007092.
- Jougnot, D., Linde, N., Revil, A. & Doussan, C., 2012. Derivation of soil-specific streaming potential electrical parameters from hydrodynamic characteristics of partially saturated soils, *Vadose Zone J.*, **11**(1), 272–286.
- Jougnot, D., Rubino, J.G., Carbajal, M.R., Linde, N. & Holliger, K., 2013. Seismoelectric effects due to mesoscopic heterogeneities, *Geophys. Res. Lett.*, **40**(10), 2033–2037.
- Jouniaux, L. & Pozzi, J.-P., 1995. Streaming potential and permeability of saturated sandstones under triaxial stress: consequences for electrotelluric anomalies prior to earthquakes, *J. geophys. Res.*, **100**, 10 197–10 209.
- Kulesa, B., Murray, T. & Rippin, D., 2006. Active seismoelectric exploration of glaciers, *Geophys. Res. Lett.*, **33**, L07503, doi:10.1029/2006GL025758.
- Kumar, P. & Foughla-Georgiou, E., 1997. Wavelet analysis for geophysical applications, *Rev. Geophys.*, **35**(4), 385–412.
- Lebedev, M. et al., 2009. Direct laboratory observation of patchy saturation and its effects on ultrasonic velocities, *Leading Edge*, **28**(1), 24–27.
- Lo, W., Sposito, G. & Majer, E., 2005. Wave propagation through elastic porous media containing two immiscible fluids, *Water Resour. Res.*, **41**, 2025, doi:10.1029/2004WR003162.
- Mallat, S. & Zhong, S., 1992. Characterization of signals from multiscale edges, *IEEE Trans. Pattern Anal. Mach. Intell.*, **14**(7), 710–732.
- Masson, Y.J. & Pride, S.R., 2007. Poroelastic finite difference modeling of seismic attenuation and dispersion due to mesoscopic-scale heterogeneity, *J. geophys. Res.: Solid Earth*, **112**, 3204, doi:10.1029/2006JB004592.
- Mavko, G. & Nolen-Hoeksema, R., 1994. Estimating seismic velocities at ultrasonic frequencies in partially saturated rocks., *Geophysics*, **59**(2), 252–258.
- Parkhomenko, I. & Tsze-San, C., 1964. A study of the influence of moisture on the magnitude of the seismoelectric effect in sedimentary rocks by a laboratory method, *Bull. (Izv.) Acad. Sci., USSR, Geophys. Ser.*, **2**, 115–118.
- Perrier, V., Philipovitch, T. & Basdevant, C., 1995. Wavelet spectra compared to fourier spectra, *J. Math. Phys.*, **36**, 1506–1519.
- Pride, S., 1994. Governing equations for the coupled electromagnetics and acoustics of porous media, *Phys. Rev. B*, **50**, 15 678–15 695.
- Pride, S. & Haartsen, M.W., 1996. Electrostatic wave properties, *J. acoust. Soc. Am.*, **100**, 1301–1315.
- Reppert, P.M., Morgan, F.D., Lesmes, D.P. & Jouniaux, L., 2001. Frequency-dependent streaming potentials, *J. Coll. Interface Sci.*, **234**, 194–203.
- Revil, A. & Cerepi, A., 2004. Streaming potentials in two-phase flow conditions, *Geophys. Res. Lett.*, **31**(11), doi:10.1029/2004GL020140.
- Revil, A. & Jardani, A., 2010. Seismoelectric response of heavy oil reservoirs: theory and numerical modelling, *Geophys. J. Int.*, **180**(2), 781–797.
- Revil, A. & Mahardika, H., 2013. Coupled hydromechanical and electromagnetic disturbances in unsaturated porous materials, *Water Resour. Res.*, **49**(2), 744–766.
- Revil, A., Linde, N., Cerepi, A., Jougnot, D., Matthäi, S. & Finsterle, S., 2007. Electrokinetic coupling in unsaturated porous media, *J. Colloid Interface Sci.*, **313**, 315–327.
- Revil, A., Barnier, G., Karaoulis, M., Sava, P., Jardani, A. & Kulesa, B., 2014. Seismoelectric coupling in unsaturated porous media: theory, petrophysics, and saturation front localization using an electroacoustic approach, *Geophys. J. Int.*, **196**(2), 867–884.
- Rubino, J.G. & Holliger, K., 2012. Seismic attenuation and velocity dispersion in heterogeneous partially saturated porous rocks, *Geophys. J. Int.*, **188**, 1088–1102.
- Santos, J., Zyserman, F. & Gauzellino, P., 2011. Numerical electroseismic modeling: a finite element approach, *Appl. Math. Comput.*, **218**(11), 6351–6374.
- Santos, J.E., Douglas, J., Jr., Corberó, J. & Lovera, O.M., 1990. A model for wave propagation in a porous medium saturated by a two-phase fluid, *Acoust. Soc. Am. J.*, **87**, 1439–1448.
- Schakel, M. & Smeulders, D., 2010. Seismoelectric reflection and transmission at a fluid/porous-medium interface, *J. acoust. Soc. Am.*, **127**, 13, doi:10.1121/1.3263613.
- Schakel, M., Smeulders, D., Slob, E. & Heller, H., 2011a. Seismoelectric interface response: experimental results and forward model, *Geophysics*, **76**(4), N29–N36.
- Schakel, M., Smeulders, D., Slob, E. & Heller, H., 2011b. Laboratory measurements and theoretical modeling of seismoelectric interface response and coseismic wave fields, *J. appl. Phys.*, **109**(7), 074 903–074 903.
- Sénéchal, P., Garambois, S. & Bordes, C., 2010. Feasibility of acoustic imaging for in-situ characterization of subsurface soil injected with fresh mortar, *J. appl. Geophys.*, **72**(3), 184–193.
- Strahser, M., Jouniaux, L., Sailhac, P., Matthey, P.-D. & Zillmer, M., 2011. Dependence of seismoelectric amplitudes on water content, *Geophys. J. Int.*, **187**(3), 1378–1392.
- Strahser, M.H., Rabbel, W. & Schildknecht, F., 2007. Polarisation and slowness of seismoelectric signals: a case study, *Near Surf. Geophys.*, **5**(2), 97–114.
- Tardif, E., Glover, P.W. & Ruel, J., 2011. Frequency-dependent streaming potential of Ottawa sand, *J. geophys. Res.: Solid Earth (1978–2012)*, **116**(B4), doi:10.1029/2010JB008053.
- Teja, A.S. & Rice, P., 1981. Generalized corresponding states method for viscosities of liquid mixtures, *Ind. Eng. Chem. Fundament.*, **20**, 77–81.
- Thompson, A.H. & Gist, G.A., 1993. Geophysical applications of electrokinetic conversion, *Leading Edge*, **12**, 1169–1173.
- Tuncay, K. & Corapcioglu, M.Y., 1996. Body waves in poroelastic media saturated by two immiscible fluids, *J. geophys. Res.*, **101**, 25 149–25 160.
- Walton, K., 1987. The effective elastic moduli of a random packing of spheres, *J. Mech. Phys. Solids*, **35**, 213–226.
- Warden, S., Garambois, S., Sailhac, P., Jouniaux, L. & Bano, M., 2012. Curvelet-based seismoelectric data processing, *Geophys. J. Int.*, **190**(3), 1533–1550.
- Warden, S., Garambois, S., Jouniaux, L., Brito, D., Sailhac, P. & Bordes, C., 2013. Seismoelectric wave propagation numerical modelling in partially saturated materials, *Geophys. J. Int.*, **194**(3), 1498–1513.
- Zhu, Z. & Toksöz, M.N., 2003. Crosshole seismoelectric measurements in borehole models with fractures, *Geophysics*, **68**(5), 1519–1524.
- Zhu, Z. & Toksöz, M.N., 2005. Seismoelectric and seismomagnetic measurements in fractured borehole models, *Geophysics*, **70**(4), F45–F51.
- Zhu, Z., Haartsen, M.W. & Toksöz, M., 2000. Experimental studies of seismoelectric conversions in fluid-saturated porous media, *J. geophys. Res.: Solid Earth (1978–2012)*, **105**(B12), 28 055–28 064.
- Zyserman, F.I., Gauzellino, P.M. & Santos, J.E., 2010. Finite element modeling of shte and psvtm electroseismics, *J. appl. Geophys.*, **72**(2), 79–91.
- Zyserman, F.I., Gauzellino, P.M. & Santos, J.E., 2012. Numerical evidence of gas hydrate detection by means of electroseismics, *J. appl. Geophys.*, **86**(0), 98–108.

APPENDIX A: DYNAMIC TRANSFER FORMULATION AS A FUNCTION OF SATURATION S_w

We present the set of equations used in our analytical calculations of dynamic and low frequency transfer functions. These equations are derived from the original work of Pride (1994) and Pride & Haartsen (1996) whose formulations were written for a fluid-filled porous medium. We extend Pride's models to a partially fluid saturated medium using an effective model, the main assumption being that we are dealing with seismic waves which wavelengths are much larger than fluid heterogeneities. We follow a similar approach to what has been done in Garambois & Dietrich (2001), Barrière *et al.* (2012) and Warden *et al.* (2013).

The input parameters are defined and listed in Tables 1 and 3:

- (i) Fluid: $\rho_w, \eta_w, K_w, \sigma_w, \rho_g, \eta_g, K_g$, (seven parameters);
- (ii) Solid: ρ_s, K_s , (two parameters);
- (iii) Porous medium: $\phi, k_0, \gamma_0, K_D, G, C_{ek}(S_w = 1), f(S_w), m, n$. (nine parameters),

where subscripts w and g , respectively, refer to water and gas. These parameters are then combined to lead to the dynamic and low frequency transfer functions for P and S waves derived below.

The variation of the poroelastic moduli of the medium H, M, C versus water saturation S_w are computed using a combination of parameters including K_f, B, K_U , following:

$$\begin{aligned} K_f(S_w) &= 1 / \left(\frac{S_w}{K_w} + \frac{1-S_w}{K_g} \right), \\ B(S_w) &= \frac{1/K_D - 1/K_s}{1/K_D - 1/K_s + \phi(1/K_f(S_w) - 1/K_s)}, \\ K_U(S_w) &= \frac{K_D}{1 - B(S_w)(1 - K_D/K_s)}, \\ C(S_w) &= B(S_w)K_U(S_w), \\ \alpha(S_w) &= \frac{1 - K_D/K_U(S_w)}{B(S_w)}, \\ M(S_w) &= \frac{B(S_w)K_U(S_w)}{\alpha(S_w)}, \\ H(S_w) &= K_U(S_w) + \frac{4}{3}G. \end{aligned} \quad (A1)$$

The effective fluid density and the bulk density of the porous medium are respectively computed as follows:

$$\begin{aligned} \rho_f(S_w) &= (1 - S_w)\rho_g + S_w\rho_w, \\ \rho(S_w) &= \phi\rho_f(S_w) + (1 - \phi)\rho_s, \end{aligned}$$

while the effective fluid viscosity is expressed by the Teja & Rice (1981) relation:

$$\eta_f(S_w) = \eta_g \left(\frac{\eta_w}{\eta_g} \right)^{S_w}. \quad (A2)$$

Neglecting surface conductivities, we use the effective electrical conductivity of the porous medium:

$$\sigma(S_w) = \frac{\phi\sigma_w}{\gamma_0 S_w^{-n}}, \quad (A3)$$

where n is the second Archie's coefficient. The frequency dependent dynamic permeability k , effective density $\tilde{\rho}$, complex density ρ_t and

effective electrical permittivity $\tilde{\epsilon}$ are respectively computed as:

$$\begin{aligned} k(S_w, \omega) &= k_0 \left[\left(1 - i \frac{\omega}{\omega_c(S_w)} \frac{4}{m} \right)^{\frac{1}{2}} - i \frac{\omega}{\omega_c(S_w)} \right]^{-1}, \\ \tilde{\rho}(S_w, \omega) &= \frac{i}{\omega} \frac{\eta(S_w)}{k(S_w, \omega)}, \\ \rho_t(S_w, \omega) &= \rho(S_w) - \frac{\rho_f^2(S_w)}{\tilde{\rho}(S_w, \omega)}, \\ \tilde{\epsilon}(\omega) &= \frac{i}{\omega} \sigma(S_w). \end{aligned} \quad (A4)$$

The frequency dependent electro-kinetic coupling coefficient L is computed as:

$$\begin{aligned} L(S_w, \omega) &= L_0(S_w) \left[1 - i \frac{\omega}{\omega_c(S_w)} \frac{m}{4} \right]^{-\frac{1}{2}} \\ &= -\frac{\phi}{\gamma_0} \sigma_w S_w^n C_{ek}(S_w = 1) f(S_w) \left[1 - i \frac{\omega}{\omega_c(S_w)} \frac{m}{4} \right]^{-\frac{1}{2}}, \end{aligned} \quad (A5)$$

where the Biot critical pulsation ω_c is obtained from eq. (5) by the relation $\omega_c = 2\pi f_c$ and $f(S_w)$ are given in Appendix B for various models.

In the following, the dependance of the parameters to S_w and ω are not all explicitly written for clarity. The slowness of the fast P waves s_P and the slowness of the S waves s_S are respectively computed as:

$$\begin{aligned} s_P(S_w, \omega) &= \left[\frac{1}{2}\gamma - \frac{1}{2}\sqrt{\gamma^2 - \frac{4\tilde{\rho}\rho}{MH - C^2} \left(\frac{\rho_t}{\rho} + \frac{\tilde{\rho}L^2}{\tilde{\epsilon}} \right)} \right]^{1/2}, \\ s_S(S_w, \omega) &= \left[\frac{1}{2}\frac{\rho_t}{G} + \frac{1}{2}\mu\tilde{\epsilon} \left(1 + \frac{\tilde{\rho}L^2}{\tilde{\epsilon}} \right) \right. \\ &\quad \left. + \frac{1}{2}\sqrt{\left[\frac{\rho_t}{G} - \mu\tilde{\epsilon} \left(1 + \frac{\tilde{\rho}L^2}{\tilde{\epsilon}} \right) \right]^2 - 4\mu\frac{\rho_f^2 L^2}{G}} \right]^{1/2} \\ \text{with } \gamma(S_w, \omega) &= \frac{\rho M + \tilde{\rho}H \left(1 + \tilde{\rho}L^2/\tilde{\epsilon} \right) - 2\rho_f C}{HM - C^2}. \end{aligned} \quad (A6)$$

Finally, the dynamic transfer function for P and S -waves, respectively $\psi_{P\text{-dyn}}$ and $\psi_{S\text{-dyn}}$, are given by:

$$\begin{aligned} \psi_{P\text{-dyn}}(S_w, \omega) &= \frac{E}{\ddot{U}_P} = \left(i \frac{\tilde{\rho}L}{\omega\tilde{\epsilon}} \right) \left(\frac{Hs_P^2 - \rho}{Cs_P^2 - \rho_f} \right), \\ \psi_{S\text{-dyn}}(S_w, \omega) &= \frac{E}{\ddot{U}_S} = \left(i \frac{\mu\tilde{\rho}GL}{\omega\rho_f} \right) \left(\frac{s_S^2 - \rho/G}{s_S^2 - \mu\tilde{\epsilon}} \right), \end{aligned} \quad (A7)$$

and the corresponding low frequency transfer functions $\psi_{P\text{-lf}}$ and $\psi_{S\text{-lf}}$ become:

$$\begin{aligned} \psi_{P\text{-lf}}(S_w) &= -C_{ek}(S_w = 1) f(S_w) \rho_f \left(1 - \frac{\rho}{\rho_f} \frac{C}{H} \right), \\ &= \psi_0(S_w) \left(1 - \frac{\rho}{\rho_f} \frac{C}{H} \right), \\ \psi_{S\text{-lf}}(S_w, \omega) &= -C_{ek}(S_w = 1) f(S_w) \rho_f \left(-i \frac{\mu}{\omega} \frac{G}{\rho} \frac{\phi}{\gamma_0} \sigma_w \right). \end{aligned} \quad (A8)$$

The complete set of eqs (A1)–(A8) rely on a few hypotheses and approximations compared to the original Pride's formulation. Here are some justifications:

(i) We neglect the surface conductivities and use a reduced version of the electrical conductivity $\sigma(S_w)$ in eq. (A3) compared to a more general expression of the dynamic electrical conductivity $\sigma(S_w, \omega) = \frac{\phi}{\gamma_0} S_w^n \sigma_w + 2 \frac{\phi}{\gamma_0} \frac{C_{em} + C_{os}(\omega)}{\Lambda}$ (e.g. Warden *et al.* 2013). Using such reduced formulation, we assume that the electromigration C_{em} and electroosmotic C_{os} conductances as defined in Pride (1994) are negligible in the calculation of the dynamic electrical conductivity, as stated in Garambois & Dietrich (2001).

(ii) We use a reduced version of the effective electrical permittivity $\tilde{\varepsilon}$ in eq. (A4) compared to a more general dynamic expression $\tilde{\varepsilon}(S_w, \omega) = \varepsilon(S_w, \omega) + \frac{i}{\omega} \sigma(S_w, \omega) - \tilde{\rho}(S_w, \omega) L^2(S_w, \omega)$. We assume that we remain in the low-frequency range and diffusive regime where $\varepsilon(\omega) \ll \frac{i}{\omega} \sigma(\omega)$ (Garambois & Dietrich 2001). We also neglect for consistency the electroosmotic term $\tilde{\rho}(\omega) L^2(\omega)$ in the dynamic expression.

(iii) The static electro-coupling coefficient L_0 in eq. (A5) is multiplied by $(1 - 2 \frac{\tilde{d}}{\Lambda})$ in the Pride's version, where \tilde{d} is basically the electrical double-layer thickness and Λ is the pore-shape factor or nearly the radius of the pores. This pre-factor in L_0 is tiny (less than a tenth of a per cent) in our case and is then neglected.

(iv) The dynamic electro-kinetic coupling of Pride (1994) is defined as

$$L(\omega) = L_0 \left[1 - i \frac{\omega}{\omega_c} \frac{m}{4} \left(1 - 2 \frac{\tilde{d}}{\Lambda} \right)^2 \left(1 - i^{3/2} \frac{\tilde{d}}{\delta(\omega)} \right)^2 \right]^{-\frac{1}{2}},$$

where δ is the skin depth. For consistency with the previous hypotheses, we have also chosen to ignore both terms in parentheses since they represent again a very tiny correction to L in eq. (A5) in the frequency band of this study.

APPENDIX B: C_{ek} VALUE AS A FUNCTION OF SATURATION S_w

B1 C_{ek} at saturation $S_w = 1$

Guichet *et al.* (2003) measured experimentally the following value of the electrokinetic coefficient C_{ek} under saturated conditions in a sand very similar to the one used in this study:

$$C_{ek}(S_w = 1) = \frac{\varepsilon_0 \varepsilon_f \zeta}{\eta_f \sigma_f} = -1.14 \times 10^{-6} \text{ V Pa}^{-1}. \quad (\text{B1})$$

The saturating fluid was water ($\eta_f = 10^{-3}$ Pa s, $\varepsilon_f \simeq 80$) which electrical conductivity was $\sigma_f = \sigma_w = 1.78 \times 10^{-2}$ S m⁻¹. Eq. (B1) then lead to a zeta potential $\zeta = -29$ mV in the sand under the experimental conditions of Guichet *et al.* (2003).

Since we have not performed any zeta potential measurements here, we have also used $\zeta = -29$ mV for our sand in saturated conditions which lead to $C_{ek}(S_w = 1) = -1.73 \times 10^{-6}$ V Pa⁻¹ (value used in Tables 1 and 3) for the conductivity of the electrolyte $\sigma_w = 1.17 \times 10^{-2}$ S m⁻¹.

B2 C_{ek} versus S_w

We detail in the following the different models giving the dependence of C_{ek} versus S_w as listed in Table 2.

Studying Fontainebleau sand (very close to Landes sand) Guichet *et al.* (2003) observed an increase of electrokinetic coefficient when

the drainage was obtained by injection of argon. They deduced an alternative model:

$$C_{ek}(S_w) = C_{ek}(S_w = 1) S_e, \quad (\text{B2})$$

where the effective water saturation $S_e = (S_w - S_{w0}) / (1 - S_{w0})$ depends on the residual water saturation S_{w0} .

Revil *et al.* (2007) proposed to express the electrokinetic coefficient as a function of the excess charge per unit of pore volume. Assuming that the surface conductivity of the rock was negligible and that the wetting phase remained continuous even for very low saturation, they proposed the following relation:

$$C_{ek}(S_w) = C_{ek}(S_w = 1) \frac{S_e^{\frac{2+3\lambda}{\lambda}}}{S_w^{n+1}} \quad (\text{B3})$$

where λ is the curve-shape parameter characterizing the pore space distribution ($\lambda = 1.7$ for sands).

In order to describe the multiphase streaming potential coupling coefficients, Jackson (2010) used a bundle of capillary tubes model occupied by two immiscible phases (oil-water or gas-water systems). If water is the only phase that contains an excess of charge, $C_{ek}(S_w)$ can be defined as:

$$C_{ek}(S_w) = C_{ek}(S_w = 1) \frac{S_e}{S_w^n}. \quad (\text{B4})$$

In this latter formulation, the residual water saturation is adjusted to S_{w0} and the surface conductivity of the rock is neglected. This model suggests that $C_{ek}(S_w)$ may increase at partial saturation before decreasing to zero at S_{w0} . This is physically plausible in case the relative electrical conductivity decreases more rapidly than the effective water saturation. Recently, Allègre *et al.* (2010, 2012) confirmed that such behaviour could be observed in silica sands with a very strong increase of $C_{ek}(S_w)$ at $S_w = 0.8$. Such behaviour is also predicted for Fontainebleau sand by Jougnot *et al.* (2012) using an alternative model also based on a bundle of capillary tubes.

B3 On the use of the CWT

This data processing computes the similarity between a theoretical wavelet seen in Fig. B1(a) and a recorded signal seen in Fig. B1(b), by comparing the original signal $s(t)$ to a shifted/compressed/stretched version of a 'mother wavelet' $w(t)$. By calculating the cross-correlation of the signal s and the wavelet w at various scales a and positions b , we obtain the $C(a, b)$ coefficients defined as:

$$C(a, b) = \frac{1}{\sqrt{a}} \int_{-\infty}^{\infty} s(t) w^* \left(\frac{t-b}{a} \right) dt, \quad (\text{B5})$$

where w^* is the complex conjugate of the wavelet function. The scale a is related to a pseudo-frequency f_a as seen in Fig. B1(c) by the relation:

$$f_a = \frac{f_0}{aT}, \quad (\text{B6})$$

where f_0 is the central frequency of the wavelet and T the sampling period of the recorded signal.

The computed spectrum in Fig. B1(d) strongly depends on the choice of the mother wavelet and corresponds to a smoothed and stretched approximation of a Fourier spectrum. CWT cannot achieve the high frequency resolution of a Fourier transform but it can however distinguish and characterize frequency properties of singular events in non stationary signals, like in our experimental data. The best spectral resolution is obtained by using mother wavelets with

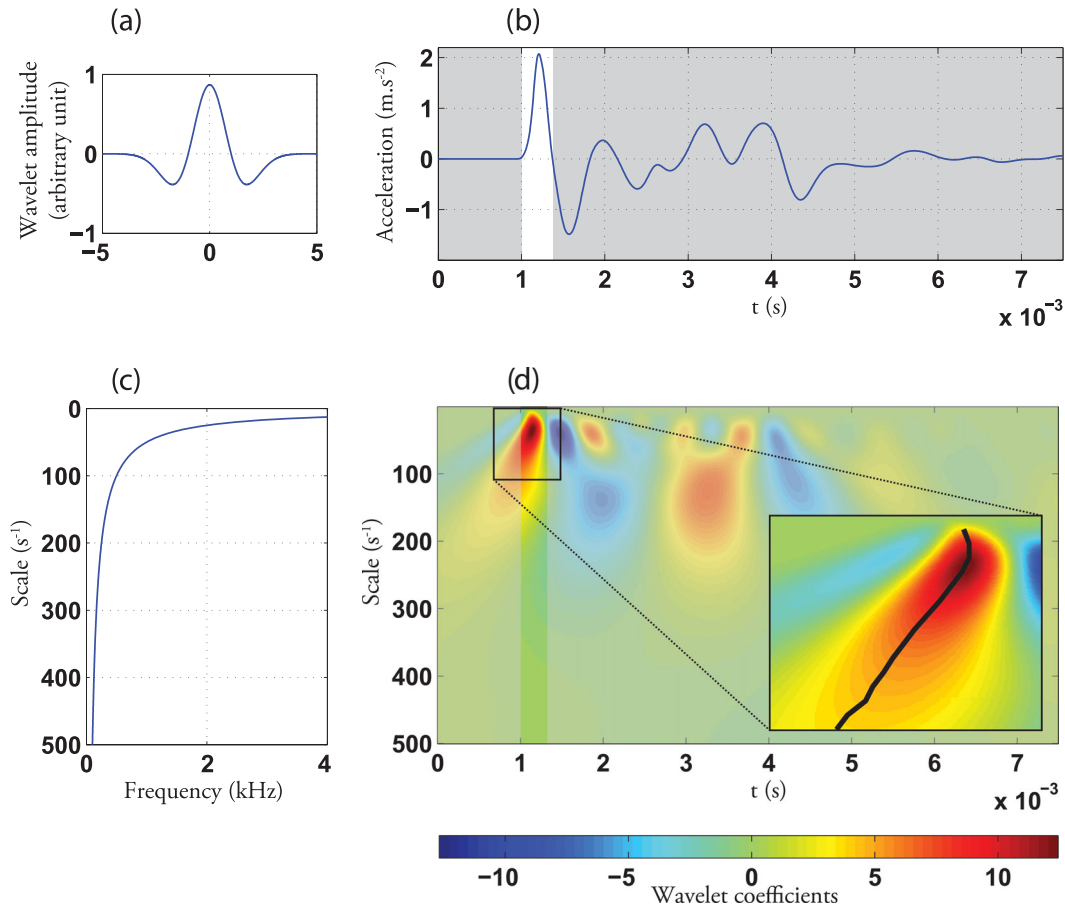


Figure B1. Example of a continuous wavelet transform (CWT) performed on seismic data. (a) Mother wavelet function chosen in this study: Mexican hat wavelet. (b) Seismic record versus time obtained during the third drainage. The first ‘lobe’ corresponding to the first arrival is highlighted. (c) Conversion from scale to frequency using eq. (B6) with $f_0 = 0.25$ Hz. (d) $C(a, b)$ spectrum map obtained by a CWT of the seismic signal shown in (b), the included figure shows the local maxima (black line) extracted to get a local spectrum. Colours indicate the amplitude of $C(a, b)$ for a given a and b .

a lot of vanishing moments (i.e. oscillations) but the time resolution obeys the opposite rule (Perrier *et al.* 1995); the choice of the mother wavelet is therefore a compromise between time and frequency resolution.

In this study, we propose to use a CWT during imbibition and drainage experiments in order to monitor the main frequencies, velocities and amplitudes of the first lobe in seismic and seismoelectric signals. We used the same wavelet for all CWT computations in order to legitimate the validity of a comparison between seismic and seismoelectric attributes.

Preliminary signal processing tests led to the conclusion that the real ‘Mexican hat’ wavelet shown in Fig. B1(a) was the most convenient wavelet to characterize in frequency the first lobe of the signal. The Mexican hat wavelet, defined as the second derivative of the gaussian function, is widely used in geophysics (Kumar & Foufoula-Georgiou 1997). As an example, we have applied the continuous Mexican hat wavelet transform to one seismic record obtained during the third drainage ($S_w = 0.9$); the derived $C(a, b)$ map is presented in Fig. B1(d).